Bolt Fatigue Failure within Cable Protection Systems

Exploring a Novel Method for Fatigue Calculations within Subsea Areas

Master Thesis

J.B.L. Zwennes

TUDelft

Bolt Fatigue Failure within Cable Protection Systems

Exploring a Novel Method for Fatigue Calculations within Subsea Areas

by

J.B.L. Zwennes

to obtain the degree of Master of Science

at the Delft University of Technology,

to be defended publicly on 23/08/2024

Student number:	4560345	
Graduation committee:	Dr. K. Anupam	TU Delft, Chair, Supervisor
	Dr. Z Yang	TU Delft, External
	Ir. C. Wang	TU Delft, External
	Ir. P. Marcus	Offshore Independents, Company supervisor

Faculty of Mechanical, Maritime and Materials Engineering (3mE) ·
Delft University of Technology

Executive Summary

The expansion of offshore wind energy has significantly increased the number of wind turbines installed in oceans. Consequently, the infrastructure needed to support these turbines, especially subsea cables, has also rapidly expanded. Subsea cables are key components, as they allow for the transmission of electricity. In most cases, the subsea cable is buried between wind turbines, but where it cannot be buried, it is subjected to movements due to the environmental loads. The movements of the cable are typically the largest where the cable touches scour protection and, in the bend, where the cable is positioned upwards and enters a subsea structure. For this reason, typically in this location, a CPS (Cable Protection System) is added, designed to protect the subsea cable during its entire lifetime. However, experience has revealed that CPS failures are not uncommon, nor are they limited to a specific design or location. Several wind farm developers have already run into costly CPS repair bills, and CPS related problems are expected to result in further financial losses over the next decade.

To effectively mitigate the risk of CPS failure, a better understanding of their failure causes is needed. However, the CPS is often quickly removed and replaced without an analytical investigation to minimize costs and downtime. Additionally, CPS manufacturers are reluctant to share knowledge about the causes of CPS failure.

Although, no publicly available numbers are available on all the root causes of the CPS failure. A known failure mode of the CPS is the abrasion with the seabed. Additionally, industry insights suggest that while the components of the CPS generally remain intact, instances of detachment or displacement along the cable have been observed. This could suggest that the bolted connections which keep the components together have failed. The integrity of these bolts is crucial as failure of one bolt could lead to instability, potentially leading to a failure of the entire system. However, assessing the fatigue life of bolts within subsea structures is challenging due to the irregular environmental loadings. To address this, a methodology has been developed that combines the capabilities of a hydrodynamic model with a detailed FEM structural model. This allows for an assessment of the damage for each sea state.

A developed hydrodynamic model, which simulates the latched CPS within a subsea environment, provided insights into the loadings of the CPS. The model showed that waves perpendicular to the CPS provide the largest loading fluctuations. Additionally, it was found that the highest bending moments and shear forces were particularly visible near the entry hole, where the latching knuckle is located and secured by bolts. Consequently, this component was identified as having a potential risk for bolt fatigue failure. A structural model was developed to assess the bolts within this component.

The fatigue results, obtained using the widely employed nominal stress approach, indicated no damage to the bolt under regular sea state conditions. Minor damage was only found in the less frequently occurring severe sea states. This led to an estimated fatigue lifetime of the bolts that significantly exceeded the allowable fatigue life. Therefore, within the scope of this research, the bolts do not form a significant risk of failure for the CPS.

Although the risk of bolt failure could not be demonstrated, the research is valuable due to its new approach. The proposed methodology for analyzing the fatigue life of bolts within the CPS provides a framework for processing environmental loadings in fatigue analysis of components. This is not only applicable for the CPS knuckle but can also be extended for other sections of the CPS or to other applications subjected to environmental loading conditions. To further refine the methodology, future research could integrate additional factors, such as Vortex-Induced Vibration VIV.

Acknowledgement

I would like to express my gratitude to those who have supported and helped me throughout my thesis journey.

First of all, I would like to thank Kumar Anupam, the chair of the committee and daily supervisor, for his support, patience, and knowledge. His experience in academic writing has been crucial, helping me learn and significantly improve my thesis. His guidance and insights delivered more structure to the thesis, which has greatly contributed to the research and writing process.

I would like to extend my thanks to the rest of my thesis committee, Chen Wang and Zhen Yang, for the friendly discussions, insightful comments and time.

I would also like to thank Pepijn Marcus, whose expertise was invaluable for my thesis. His insights, industry experience and extensive knowledge provided a comprehensive understanding throughout this journey. During our weekly meetings, he always showed patience and willingness to explain things multiple times, when I did not understand them initially. Despite his busy schedule, he always made time for me. In addition, his experienced perspective on the research topic, allowed me to critically refine my initial approach, which contributed to the successful completion of my thesis.

In addition, I would like to show my gratitude to all the people of Offshore Independents. From day one, they made me feel like part of the team. I genuinely believe that the company holds something unique. The combination of impressive intern knowledge, a supportive atmosphere, trust, and a wide variety of cultures and friendships all contributed to making my graduation experience significantly more enjoyable.

Lastly, I want to thank the people who are special to me, including my family, friends, and roommates. Your willingness to offer a listening ear during the graduation process, which I often found challenging, made a significant difference, for which I am truly grateful.

Thank you all.

Contents

List of Figures

List of Tables

List of Abbreviations

ABR Articulated Bend Restrictor.

CPS Cable Protection System.

DFF Design Fatigue Factor.

FEM Finite Element Method.

FLS Fatigue Limit State.

HISC Hydrogen Induced Stress Cracking.

LAT Lowest Astronomical Tide.

MBR Minimum Bend Radius.

MSE Mean Squared Error.

SCF Stress Concentration Factor.

ULS Ultimate Limit State.

VIV Vortex-Induced Vibration.

1

Introduction

This chapter provides the motivation and relevance of the research and discusses the current problem regarding the failure of the Cable Protection System (CPS). It continues by outlining the research questions, which will serve as the foundational framework for this study. The scope of research is specified, and its limitations will be addressed.

1.1. Motivation & Relevance

The growth of the world population results in a significant growth in energy demand. The urgency of the energy transition from the mainly used fossil fuel towards renewable energy, with low to zero-carbon emissions, has been emphasized in the previous study [1]. The reduced costs and improved competitiveness of renewable power, including wind energy, provide an opportunity to accelerate the energy transition [2].

Nevertheless, there are still challenges in the renewable industry. In recent report [3], the number of claims in the offshore wind sector related to cable issues represents over half of the insurance claims. Another report [4] even states that 75% of the insurance claims are due to subsea cable issues. While the exact number of claims related to the failure of the CPS is not specified, it is clear that the failure of the CPS is not uncommon. The world's largest offshore wind developers have encountered CPS issues. Ørsted, for example, disclosed CPS malfunctions at ten of their offshore wind farms, and other major developers like Vattenfall and RWE have also identified CPS issues at their wind farms [5]. The urge to find solutions for these CPS failures, thereby reducing the subsea cable losses, is strong.

1.2. Problem Statement

The main problem concerning the failure of the CPS is that the root causes of failure remain difficult to determine. This is largely due to the scarcity of open data and available literature on the root causes of CPS failure. When failure at a CPS has been detected, the focus often lies on solving the issue rather than investigating the root causes [4]. The CPS is often quickly removed and replaced, and no analytical investigation has been performed to minimize the costs and downtime. Moreover, manufacturers and wind farm developers are reluctant to share detailed information regarding the failure of the CPS.

According to industry practice [6], components of the CPS sometimes remain intact but are falling off or have slid along the subsea cable. This observation could suggest that the bolt connections which keep the components together have failed. However, no open literature or research confirms nor disproves the possibility of failure of the bolt within the CPS. This study aims to research whether bolt failure presents a potential risk to the integrity of the CPS.

If it is found that the bolted connections form a risk, then this implies that already installed CPS may be susceptible to bolt failure, and preventive measurements could be sensible to apply. Insights into the causes of bolt failure can help assess where and when preventive actions should be implemented. Besides the preventive measurements, the outcome can also improve future CPS instalments. CPS designs can

be adapted to lower the risk of bolt failure.

The primary challenge within this research is the irregular bolt loadings caused by the hydrodynamic environment. While hydrodynamic models offer a viable solution to assess the loads that the CPS withstand, it does not offer an in-depth structural analysis required to evaluate the bolt loadings, as can be obtained with Finite Element Method (FEM) models. Such a comprehensive analysis is necessary to evaluate the bolt loading to estimate the fatigue lifetime of the bolts.

1.3. Research Questions
To determine whether bolt failure in the CPS poses a potential risk, the following research question has been formulated:

> *What are the critical limit states associated with the bolted connections within the cable protection system in subsea environments?*

To answer this question, it is split into the following four sub-questions:

1. What are the critical locations within a cable protection system where the bolted connections are most susceptible to failure?
2. What fatigue limit states could potentially compromise the integrity of these bolted connections?
3. How do various loading and movement conditions affect the bolted connections within the system?
4. Based on the proposed methodology, what can be said about the expected lifetime of the bolts?

1.4. Plan of Approach
The methodology, provided in chapter 3, is unique in the existing literature and allows for examining the Fatigue Limit State (FLS) for bolts at the most susceptible locations within the CPS. An interaction between the hydrodynamic model and the structural model is used to examine the FLS.

To answer the first sub-question of finding the most susceptible bolts to failure, the fluctuations of loads obtained from the hydrodynamic model can be assessed.

To address the sub-question concerning the relevant limit states of bolts and the transfer of loads and movements to the bolted connection, the loads derived from the hydrodynamic model can be applied to a structural FEM model. This application enables an assessment of the relevant limit state concerning the bolts and allows for the effects of the global loads on the bolts.

To address the last sub-question regarding the expected lifetime of the bolt. A correlation between loadings at the CPS and the bolt loads could be found. This correlation allows for the fatigue calculations for each of the sea states. And since the probability of occurrence is known, the expected lifetime could be assessed within the scope of the research.

This approach offers a methodological framework for conducting other fatigue analyses in subsea environments. However, it is important to note that this analysis is based on numerous assumptions due to the scarcity of openly available data from the industry.

1.5. Scope of Research
This research is focused on the use of CPSs at fixed offshore wind turbines. However, the use of CPSs systems is not limited to offshore wind. Other Applications, like platform umbilicals and offshore substations, make use of similar systems [7].

In terms of external loading, only the interaction between waves and current is considered. Vortex-Induced Vibration (VIV), a phenomenon where oscillations are induced in a structure due to fluid flow, is not included. Despite the potential impact of these VIVs on the structure's lifespan, it falls outside the scope of this study.

The assessment of the CPS will be considered after installation. The CPS model that will be considered will already be latched in the entry hole of the monopile. This means that the loads that occur during the installation phase fall outside the scope of this research. While these pull-in operations involve various

forces and movements, modelling them would significantly complicate the analysis. It is important to recognize that damage could occur during the installation process.

Lastly, thermal fatigue is not considered within the scope of this research, despite the potential thermal fluctuations from the heating of the power cable and sea temperature differences.

1.6. Limitations of Research

There are several CPS manufacturers, each with its own different CPS design. This research will, however, be looking at one generic model of a CPS. This generic model will be based on leading CPS designs in the industry [8].

Scour formation at the seabed could lead to a longer section of the CPS being exposed or free-spanning, which could lead to increased forces generated on the cable and CPS system, which could result in more damage [4]. However, since scour formation depends on various factors and does not consistently occur, it is not considered in this study.

When utilizing the S-N curve, the mean stress can impact the fatigue life. The obtained S-N curves from the standard experiments are often done with fully reversed cyclic loading. Nevertheless, fatigue loading is not always fully reversed, and the normal mean stresses can also affect how components behave. Consequently, methods are available to shift the S-N curve to account for these mean stresses, a process often referred to as mean stress correction [9]. The most well-known mean stress correction methods are Goodman, Soderberg, Gerber and ASME Elliptical. These methods differ in conservatism and some are better for ductile materials, while others are for brittle [10].

However, according to Okorn [11], using mean stress corrections minimally affects a bolt's fatigue life. The notches in the thread and the associated stress concentrations play a far more crucial role. The Eurocode [12] and DNV [13], therefore, neglect the mean stress correction at bolts.

2

Literature Research

2.1. General Understanding of the CPS

The wind turbines are connected to each other with an inter-array cable. The transmission of electricity to shore is done with a higher capacity cable with an export cable [14]. An overview of the cabling for a fixed offshore wind turbine is shown in Figure 2.1. It shows how the electricity gets transmitted from the wind turbine towards the offshore substation and then continues with the export cable towards onshore facilities. The purpose of these submarine power cables is to transport an electric current at a high voltage. There are two types: Alternating Current (AC) and Direct Current (DC). Depending on the route length, voltage grid synchronization and the required transmission capacity, the type is chosen. Typically, when a route is less than 80km, an AC cable is used because it is the most economical. However, AC cable has a limited distance, so for longer distances, a DC cable is often used [15]. An overview of all the different components within an inter-array cable is provided in Appendix A.1.
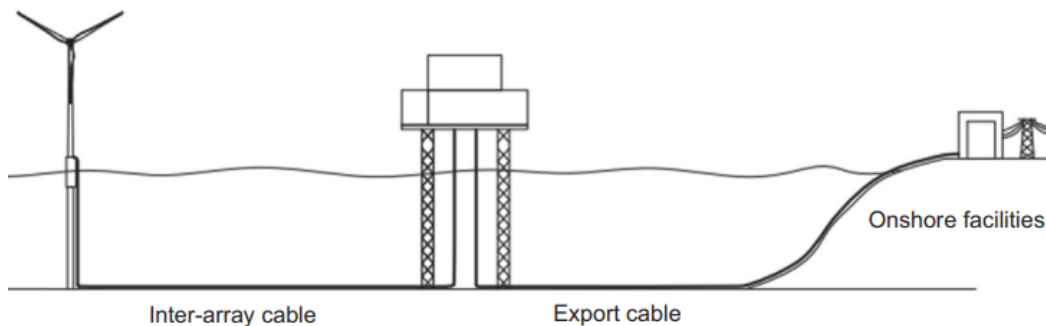
Figure 2.1: Cable overview wind turbine to shore [15]

These power cables are first carefully installed on the seabed and then often buried beneath the seabed to stabilize and protect them. However, around the monopile foundation of the wind turbine burial is not feasible since it has to enter the monopile after it has been installed. Given their critical significance, safeguarding these inter-array cables which are done by using of the CPS is there for essential [16].

In Figure 2.2, a side view of an installed CPS is provided. It shows how the CPS, latched into the entry hole of the monopile, is utilized to guard the power cable at the locations where it is able to be buried within the seabed. In addition, the CPS also plays a crucial role in securely anchoring into the monopile to prevent additional movement and ensure the integrity of the power cable.

There are different designs for and manufacturers for CPSs. Nevertheless, these CPSs typically share a similar setup. Appendix A.2 illustrates the most commonly used segments of the CPS, providing a clearer understanding of their functions.
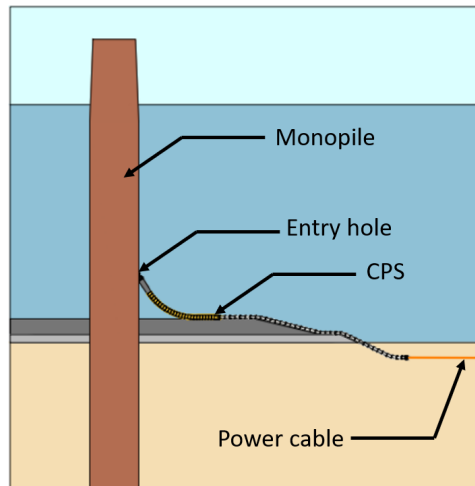
Figure 2.2: Overview Installed CPS [17]

2.2. Failures of the CPS

As highlighted in the section 1.1, the number of insurance claims within the offshore wind sector due to cable issues represents a significant part of the claims and failure of the CPS is not uncommon. However, there is a notable scarcity of open and available information in the literature regarding the failures observed at the CPSs. This makes it not possible to provide numbers or locations where the CPS failures tend to occur. This gap in the literature indicates the significance of the research. Given the limited available data, this study attempts to discuss the common failure modes based on industry experience and industry reports.

2.2.1. Abrasion

One failure mode observed in subsea cables, which is also relevant for the CPS, is abrasion. When the maximum lateral and vertical hydrodynamic loads act on the CPS are greater than the soil resistance, the CPS will move across the seabed. Due to the relative motion of the CPS across the seabed, abrasion can occur. The abrasion can be defined as material that gets removed due to the sliding of the object [18]. The type of soil on the seabed has an influence on the rate of abrasion. A hard seabed, like rock, can increase the rate of abrasion. Besides the type of soil, the severity of the lateral movement and the submerged weight influence the rate of abrasion. In the article by Durakovic [19], the root cause of the inter-array cable issues at the Race Bank wind farm is related to such abrasion of the CPSs by movement over the rock scour on the seabed. Therefore, according to the joint industry project [17] initiated by Deltares, an abrasion analysis is recommended to determine whether additional stabilization of the CPS is required.
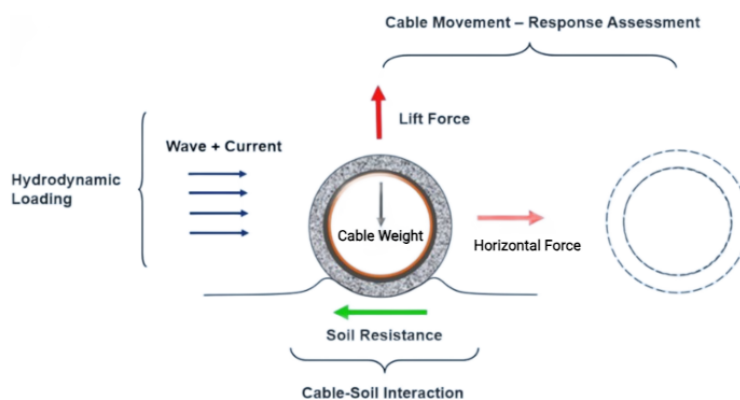
Figure 2.3: Abrasion [20]

2.2.2. Bolted Connection Failure

Although abrasion could explain failures seen at the CPS at the seabed, there are also failure locations well above the seabed, where abrasion is not identified as a plausible cause. A potential cause for this failure is the failure at the bolts, as suggested by industry experts [6]. In article [21], the importance of bolt lifetime estimation at the CPS is stated, suggesting a potential concern regarding the failure of bolts in the industry. However, the is no scientific evidence available to support this claim.

When examining the plausible locations for the bolted connections inside a CPS to fail. One area where bolt failure could happen is at the bend restrictor. The bend restrictor, shown in Figure 2.5, typically consists of half shells, which are made from polyurethane (PU). These shells are connected to each other by using bolted connections. The shells are designed to collide when enough bending occurs to restrict the part from overbending. The forces released during this collision could translate into forces in the bolts, which could result in failure due to not satisfying the FLS.

Figure 2.4: Bend Stiffener [22]

Figure 2.5: Bend Restrictor [22]

According to Felici [4], a high bending moment can be expected at the interface between the monopile or J-tube and the CPS. This provides another hypothetical location where bolt failure may occur: between the bend stiffener or bend restrictor and towards the latch unit, which is often connected by the use of a knuckle. The knuckle serves as a joint to connect different sections of the CPS. From practice [6], it has also been observed that at this transition, the CPS has detached and remains lying on top of the subsea cable. Failure of the bolts that connect these sections could explain how the CPS sections get detached from each other and result in slippage of the CPS.

It is important to note that the potential failure locations of these bolted connections lack any scientific evidence. Therefore, other reasons for failures at this location should not be excluded.

2.3. Bolts

This research will focus on examining the bolts within the CPS. This paragraph provides background information necessary for understanding how bolted connections function and potentially fail.

2.3.1. Bolt Terminology

A bolted joint is designed to hold two or more parts together. It consists of several components, as illustrated in Figure 2.6.
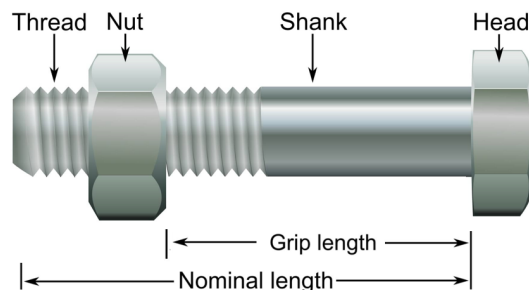
Figure 2.6: Bolt Terminology [23]

The bolt head is a flat, broad part which transfers forces to the clamp loads. The shank is the part of the bolt without any thread. The thread represents the grooves on the bolt, the nut engages with

this thread holds the assembly together and aims to prevent slippage. The nominal length is measured from below the head to the tip of the bolt. The shank between the below the head and the threaded section of the bolt is referred to as grip length [24]. In addition to the bolted joint setup, a washer can be incorporated into the setup. This component can be used to prevent the screw from loosening and help distribute the load from the nut and or bolt head over a larger area [9].

2.3.2. Bolt Loadings
There are generally three types of loading at the joints: Tension load, shear load and bending load.

(a) Tension Load   **(b)** Shear Load   **(c)** Bending Load
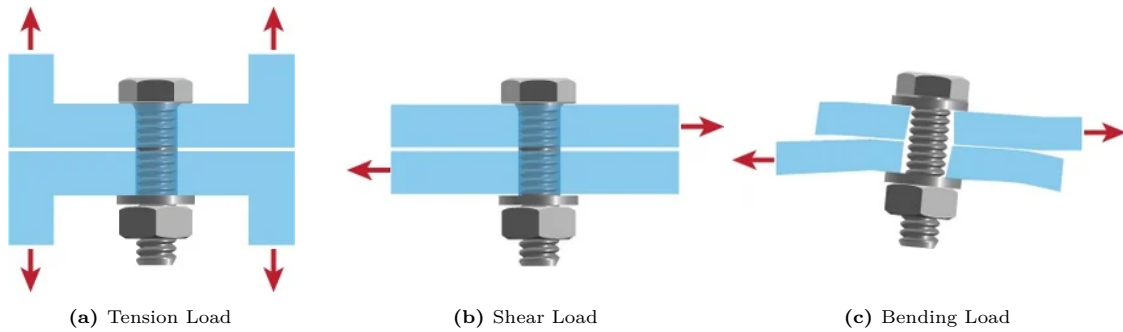
Figure 2.7: Bolt Loads [25]

The tension load is illustrated in Figure 2.7a. Tensile forces work at the bolt, causing it to stretch or separate the joint. To prevent stretching and separation of the joint a preload is often applied. Preload can be created by torquing the bolt heads or nuts. This lowers the grip length and compresses the flanges. When the working load equals the preload in the bolt, the force in the member equals zero. However, when applying more tensile forces than the preload, the bolted joint can be seen as a spring. As the spring is pulled, the spring will stretch, but after release, the spring will revert to its original shape. However, when the spring stretches too far, it remains stretched. The same mechanism is valid for the bolt, when the tensile load is higher than the preload the bolt stretches elastically, however when the stretching exceeds the elastic limit, it will plastically deform, which leads to a loss of preload. Tensile load fluctuations can occur multiple times and progressively result in a continued loss of preload and, eventually, fatigue failure. To prevent fatigue failures, the bolt designer should specify the initial preload and prevent plastic deformation in the first place [26].

The shear load, illustrated in Figure 2.7b, occurs when components slide sideways and apply force to the fastener. Some bolted connections resist the slipping of the members by using the clamped loading. This requires enough frictional force between the flanges. The friction force results from the normal force (N) between the flanges and the roughness of the contact surfaces, quantified as the friction coefficient (μ). The friction force equals the normal force times the friction coefficient (μN). Other shear joints are only depending on the shear strength. These bolts are referred to as "bearing type" joints. The tension force of these bolt joints is less important as long as the bolted connection is retained.

The bending load, illustrated in Figure 2.7c, combines both shear and tension loading. This combination can have a substantial impact on the strength and behaviour of bolted connections [26]. The strength of a bolted connection under bending loading is determined by several factors, including the material properties of the bolt and the members being connected, the size and shape of the bolt and hole, and the tightness of the bolt.

2.3.3. Bolted Joint Diagram
Bolted joint diagrams, as shown in Figure 2.8, help to understand the characteristics of the preloaded bolted joint. F represent the external load and consists of two parts: the ΔF_B part, which represents the increased load on the bolt and the ΔF_J part, which represents the reduced clamping force on the joint.
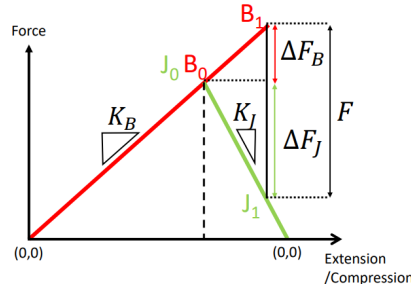
Figure 2.8: Bolted Joint Diagram [27]

2.3.4. Bolt Failure

There are mainly two ways failure at bolt can occur due to large forces [27].

The integrity of these bolts is crucial as the failure of one bolt could precipitate instability, potentially leading to a failure of the entire system [28]. Although the steel used for bolts appears robust, it is important to recognize it is an elastic material. This implies that if the bolt gets loaded, the material undergoes stretching but will typically revert to its original shape. However, if the total load is higher than the yield point, as shown in Figure 2.9a, the bolt gets permanently deformed. As deformation occurs, the stress-strain curve takes a downward path. If the bolt keeps getting stretched to the point of the ultimate tensile strength, the bolt starts "necking" and eventually fractures [9]. However, the maximum load does not always have to be reached to lead to bolt failure. The deformation, which happened prior, also decreases the clamping load. In the second failure diagram, seen in Figure 2.9b, the clamping force is insufficient. The total force is more than the clamping force, which results in a gap between the two parts. As shown, the entire external load will now need to be sustained by the bolt without any clamping force. This absence of clamping force could result in a force that is too high for the bolt, causing it to fail. When fatigue failure at the bolted connections occurs, this is frequently the result of the decreased clamping force.

(a) Yielding [27]

(b) Clamping force decreased [27]
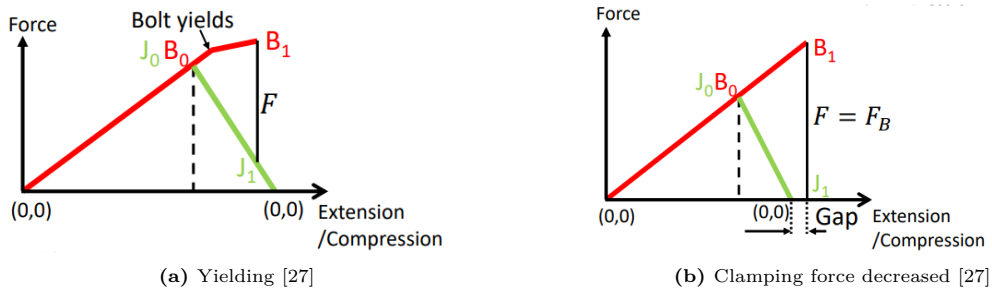
Figure 2.9: Bolt Behavior

In Lotsberg [29], it is emphasized that to prevent bolts from failing from dynamic loading, several factors should be considered in the selection of bolts. These factors include the geometry of the bolts, the steel grade or property class, the selection of corrosion protection, adherence to relevant standards, fabrication tolerances (including surface finish), and the pretension level, along with its ability to maintain the protection level.

2.4. Limit State

By considering the limit states in the design of structures, engineers can ensure that the analysed object is safe and durable and can serve its intended purpose for its entire lifespan. In structural engineering designs, the primary limit states are the Ultimate Limit State (ULS) and the Fatigue Limit State (FLS).

The ULS of an object is the highest load it can bear before breaking or sustaining irreversible damage. The load is calculated based on the strength of the materials used, the design, and the loads that the structure will be subjected to. For such a structural calculation, the encountered loads need to be

analyzed. These loads are referred to as Characteristic Loads. However, these loads could turn out to be higher than initially calculated. Therefore, design factors are applied to these characteristic loads.

To achieve greater durability, it is crucial to consider not only the highest load but also the repetitive or cyclic loadings below the highest load, as these can result in failure as well. This phenomenon is known as fatigue failure. According to research paper [30], the FLS failure accounts for 80-90% of the failures in steel structures. Given the dynamic loading conditions in the subsea environment, this limit state seems to be essential to address the impact of FLS failure. Therefore, this research will concentrate only on the FLS.

The FLS is defined by the maximum number of loading cycles a material can endure under a certain load amplitude. Due to the cyclic loading caused by the waves, fatigue is a crucial state limit for ships and offshore objects. As stated by [31], offshore structures are considered uncertain and complex. Since bolts are considered critical parts in fatigue-loaded structures, an estimation of the FLS is crucial [32].

2.4.1. Fatigue Limit State
Fatigue failure is generally split up into different stages. In the first stage of fatigue failure, a crack forms. These cracks initiate at material micro-structures or at areas with a relatively high void density [31]. The crack locations are not detectable with the naked eye and result in a higher localized stress concentration. The next phase that occurs is crack propagation, here the initiated crack continues to grow due to the cyclic loading which leads to an increased stress on the surface. The microscopic material imperfections have grown into macroscopic cracks. In the final stage, the cross-sectional area is reduced even further which weakens the part and leads to an even larger crack, the developed crack continues to grow until tensile failure occurs [9].

S-N curves
For the calculation of the FLS, the S-N curve plays a crucial role. An S-N curve, as shown in Figure 2.10, provides information about the relationship between the stress amplitude (S) on the Y-axis and the number of cycles (N) on the X-axis. A logarithmic scale is often used to represent the number of cycles. As shown in the figure, when the stress amplitude reaches the S-N curve, the fatigue life can be found.
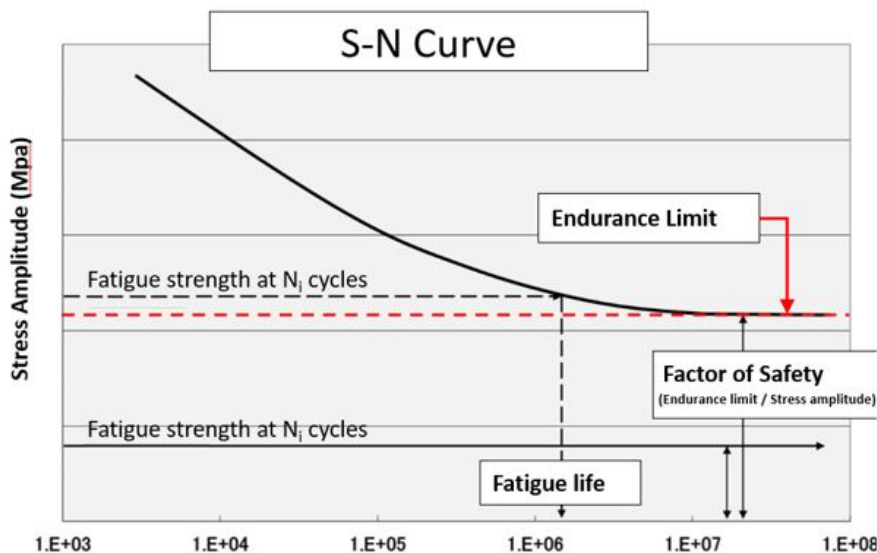
Figure 2.10: SN-Curve [33]

FLS failure occurs at the upper part of the S-N curve, and the S-N curve approaches a limit. Below this limit, the stress amplitude cannot reach the S-N curve and will, therefore, not lead to fatigue failure. This limit is referred to as the endurance limit [29]. The S-N curve is often obtained from laboratory specimens [34].

2.5. Summary Findings

In this chapter, the components are explained, continued by offering the current understanding of the possible failure modes of the CPS. Based on limited insights from the industry, a new finding was the potential risk of bolt failure within the CPS. Two plausible bolt failure locations were identified: within the bend restrictor, due to bend restrictor shells colliding against each other and near the entry hole, where high bending moments can be expected. The fatigue limit state has been identified as the crucial limit state for the bolts. However, these different sea states are leading to different stress results, and these irregular loading conditions can be complex to analyze. Therefore, a methodology, presented in chapter 3, is developed to assess the bolt fatigue life.

<div style="text-align: right; font-size: 3em;">3</div>

Methodology

Due to the irregular environmental loadings affecting the CPS, the bolts within the system are subjected to variable cyclic loading. To account for these variable cyclic loading resulting from diverse sea-states, a new method is proposed for assessing the fatigue life of the bolts in the CPS. The approach combines the benefits of a hydrodynamic model and the capabilities of a structural model.

Figure 3.1 illustrates the steps to calculate the expected bolt fatigue life. To clarify the methodology diagram, the process has been divided into three main stages: Hydrodynamic Analysis, Structural Analysis and Fatigue Limit State Analysis. These main stages correspond to the upcoming chapters.

3.1. Hydrodynamic Analysis

The CPS is deployed in a subsea environment, where it is subjected to loads from the waves and currents. To determine the loads that the CPS encounters, a hydrodynamic model is developed. This hydrodynamic model simulates the CPS latched into a monopile and allows for the application of wave and current data. To obtain the loads that the CPS encounters.

The first step to developing the hydrodynamic model involves modelling the structural specifications. The structural specifications include the necessary properties for the monopile with the scour protection, the power cable, and the CPS. The data is obtained from the industry report [8], which describes a similar CPS configuration. More modelling details are discussed in section 4.1.

After the base of the hydrodynamic model has been set up, the environmental conditions are applied. These conditions include the water depth, wave and current data obtained from the MetOcean report [35]. For the waves, the significant wave height, peak period and direction are specified. For the current, the velocity is specified, and the direction is assumed to be co-linear with the wave direction. Additionally, marine growth is added to the CPS, which increases the impact area. Further details on the application of environmental data are provided in chapter 4, which utilizes DNV [36–39]. Section 4.2 discusses the variations in environmental data and explains how the hydrodynamic model utilises these inputs to calculate the loads encountered by the CPS.

These different sea-state combinations are discussed in subsection 4.3.1. The obtained loading results, which include the shear, tension and bending moment, are analyzed along the entire CPS. Based on these results, as provided in section 4.4, and experience from the industry [6], a location for plausible bolted connection failure is selected. This section of the CPS is selected for further structural analysis. The loading results are obtained from a specified node of the CPS.

3.2. Structural Analysis

To analyze the effect on the bolts due to the encountered loads at the CPS, a structural model is developed. The setup of the model consists of five main steps. First, the geometry of the selected location of the system is modelled. The geometry of the selected part of the CPS is detailed, and the adjacent sections that geometrically are connected to the point of interest are also included. Second, the

material properties are applied to the different sections of the system, as discussed in subsection 5.1.2. Third, the contact areas are specified to ensure accurate interaction between the components, elaborated in subsection 5.1.3. Fourth, the mesh is generated and manually refined in areas where the system collides or where there are specific points of interest, such as the bolts, as discussed in subsection 5.1.4. Lastly, the model is constrained at several locations. Further details are provided in subsection 5.1.5.

After the base of the structural model has been set up, the loads are applied. First, the bolts are brought in tension in the first loading step. This applied preload is based on DNV [40], as discussed in section 5.2.

Starting from the second time step, several loading results obtained from different time moments of the hydrodynamic model are applied to the structural model. These loadings include extreme load cases obtained from the hydrodynamic model simulations, as well as random loading moments. This mixture of extreme and random loadings is made to obtain a thorough assessment, and obtaining a large data set.

After the external loads have been applied, the bolt results, which include the shear and tension stress and the workload of the bolts, are obtained and examined. The potential for shear and tensile failure is assessed.

Since the fatigue calculation is based on the nominal stress approach, only the workload is utilized since this allows the calculation of the nominal stress of the bolt. The bolt results are discussed in more detail in section 5.4.

A limited validation is conducted. Local peak stresses at the bolts are validated by comparing them to plausible failure locations. Furthermore, bolts are preloaded to their proof load, and the outcomes are compared with those found in other publications section 5.5.

3.3. Fatigue Limit State Analysis

The Fatigue Limit state analysis is performed in this study based on the nominal stress approach, as suggested by DNV [13]. It utilizes the hydrodynamic model capabilities of performing a fatigue calculation. However, the hydrodynamic model is initially not capable of obtaining the bolt stress. Therefore, an external function must be implemented within the model.

To obtain the nominal bolt stresses for each sea state, a correlation is found between the applied loads derived from the hydrodynamic model and the resulting workload from the structural model. The results of the extreme loading cases and random loading cases, which are all performed within the structural analysis, are applied to regression models.

These regression models differ in degrees and utilized loading results. The multiple regression models are tested to find the best-suiting correlation formula. The various correlation formulas obtained from the different regression models are tested using statistical measures. In section 6.2, this is discussed in more detail.

After identifying the most suitable correction formula, it is implemented within an external function code. This external function, which can be found in section E.2, enables the hydrodynamic model to calculate the nominal bolt stress in a time domain. To achieve this, the code utilizes the loading results at each time step from the specified node as input values for the correlation formula, allowing it to estimate the workload of the bolt at each time step. This estimated workload is then divided over the specified tensile stress area of the bolt to obtain the nominal stress at the bolt. The obtained loading results from the hydrodynamic time domain for the correction are discussed in section 6.3. With the external function in the hydrodynamic model, the model can calculate the nominal bolt stress for each time step.

With the nominal bolt stress in the time domain obtained, the damage can be calculated. To achieve this, a suitable S-N curve for bolts, obtained from DNV [13], is applied to the fatigue module within the hydrodynamic model. The hydrodynamic model uses the Rainflow Counting method to quantify the nominal stress cycles. The damage from each cycle is then calculated based on the specified S-N curve. The total damage caused by the series of varying stress cycles of each sea state is then determined using

the Palmgrem-Miner rule. A more detailed explanation of the damage calculation process can be found in section 6.4.

For each FLS simulation case, as specialized in subsection 4.3.1, the method is applied to obtain the total damage of each sea state case. Using the wave scatter diagram, as provided in Table 4.4, the occurrence of each sea state is known. This allows for a numerical calculation of the total damage for the specified simulation time. Since the total damage is inversely correlated to the lifetime of the bolts, it is used to estimate the fatigue life of the bolts. The results of the total lifetime of the bolts will be discussed in section 6.6.
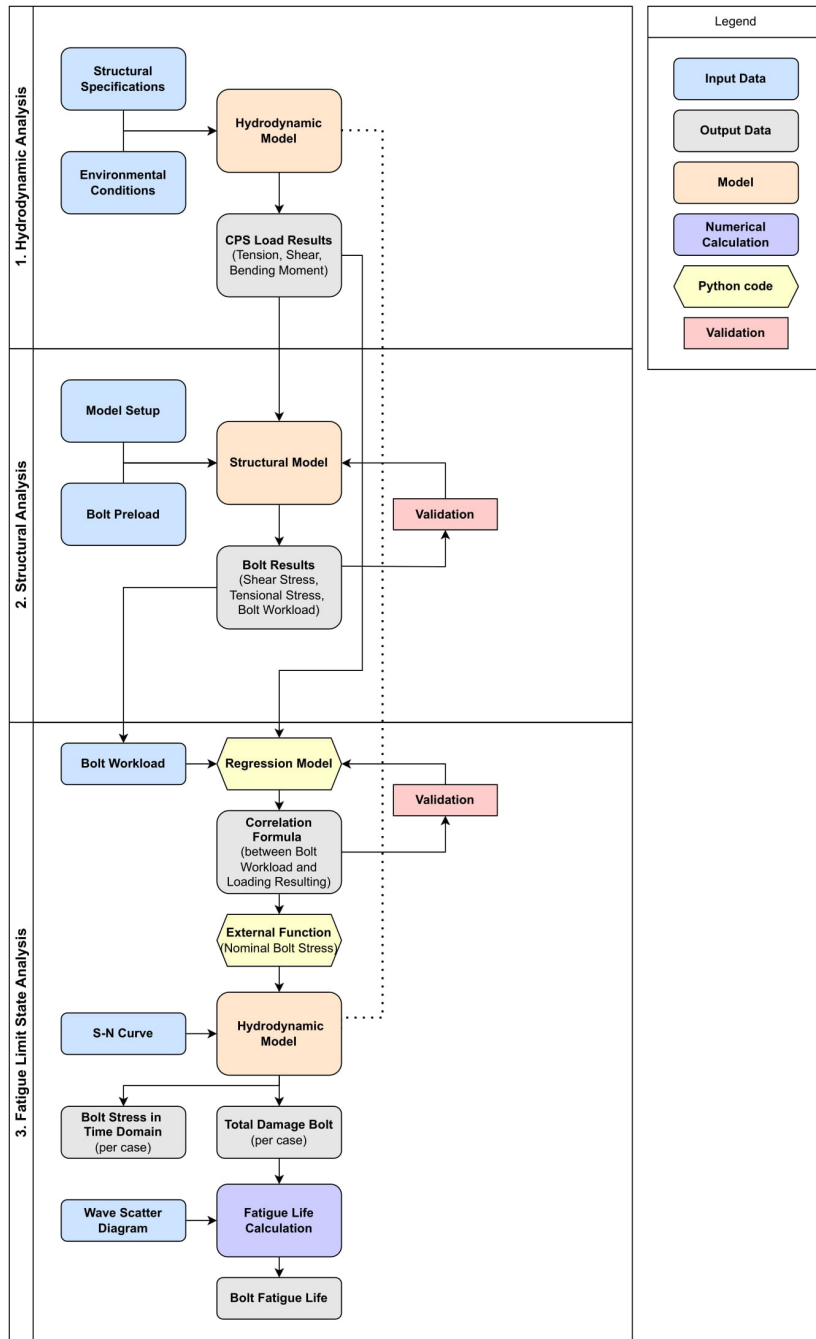
Figure 3.1: Methodology Diagram

4

Hydrodynamic Analysis

To analyze the behaviour of the CPS, a hydrodynamic analysis is performed. OrcaFlex [41] is used to conduct this hydrodynamic analysis. This software has the capability to conduct static and dynamic evaluations for offshore structures. It is designed to handle a wide range of applications, including obtaining various loading results of an CPS. This chapter elaborates on how the hydrodynamic model has been set up and which environmental data has been implemented. Furthermore, it provides insights into how the data is utilized within the hydrodynamic model to obtain the required results.

4.1. Structural Specifications

In Figure 4.1, a 3D view of the hydrodynamic model is provided. The figure illustrates the monopile with the CPS latched into it and the subsea cable extending upwards inside the monopile. The power cable is modelled until up to the hang-off clamp, where it is secured. In the right corner of the figure, a global coordinate system is provided. This global coordinate system is shown in all figures to define the positions and orientations of objects within a model.
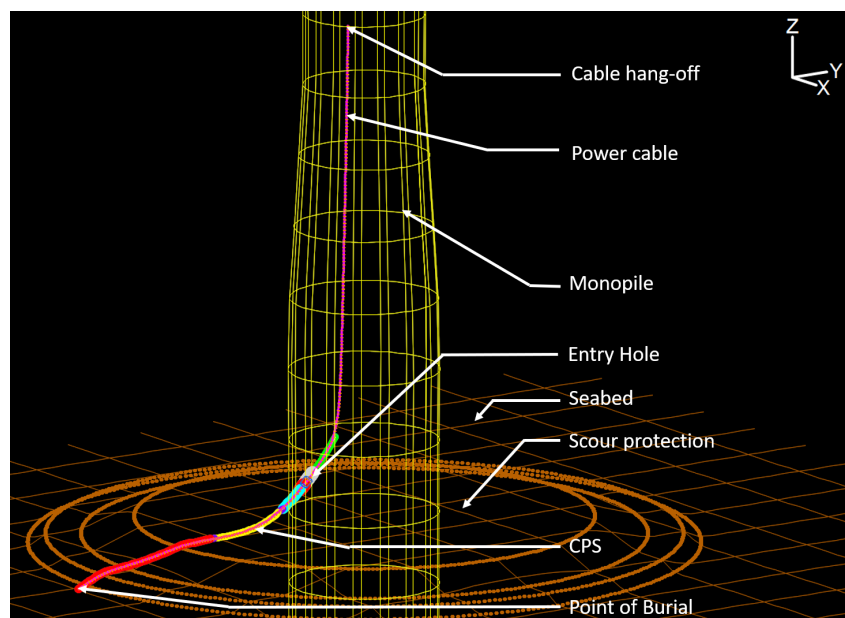
Figure 4.1: Overview Hydrodynamic Model

4.1.1. Monopile and Scour Protection

In the hydrodynamic model, the monopile is modelled with a base diameter of 8.5 meters, sloping to 7.0 meters at the sea surface. These diameter values are obtained from industry report [8]. The monopile is modelled as trapped water, which suppresses the fluid motion within the monopile [42].

The foundation of an offshore wind turbine is typically installed with scour protection to prevent scour at the seabed. The scour protection often consists of two rock layers: an armour layer and a filter layer. Both these layers are included in the hydrodynamic model. The armour layer is modelled with a diameter of 13.0 meters, a slope of 1:3 and a thickness of 1.0 meters. The filter layer is modelled with a diameter of 18 meters, a slope of 1:2 and a thickness of 0.5 meters, which is based on report [8]. In Figure 4.2, the dimensions of the monopile and scour protection are shown.
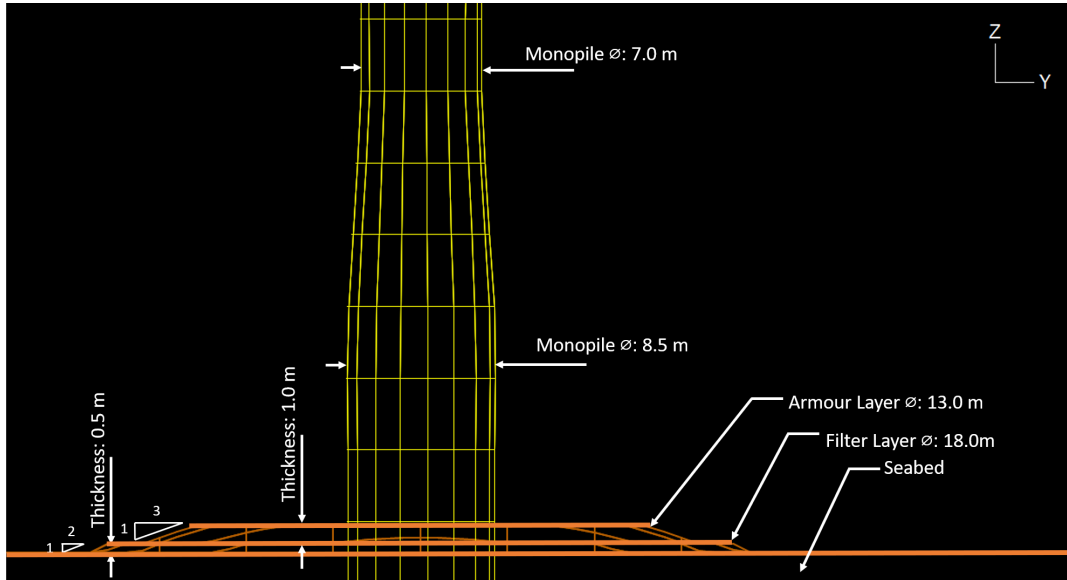
Figure 4.2: Dimensions Monopile and Scour Protection

Material	Friction Coefficient
Sand	0.6
Rock	0.6

Table 4.1: Friction Seabed Coefficient

The scour protection is installed prior to the installation of the CPS, causing the CPS to rest on top of the scour protection. Therefore, addressing the friction between the scour protection and the CPS is crucial. In the hydrodynamic model, the seabed friction coefficient, as defined by DNV [43], is shown in Table 4.1. While these coefficients are utilized in the model to account for the friction, it is worth mentioning that these values do not consider the potential of the CPS locking between the rocks on the scour protection. Consequently, these friction coefficients are considered low and overly conservative.

4.1.2. CPS Data

The model of the CPS is based on a CPS design, which is one of the leading designs used in the industry. The generic CPS model consists of different sections, as shown in Appendix A.2. The different sections, are shown in Figure 4.3

Given that the CPS consists of different sections, multiple line types were used for each part of the section in the configuration of the CPS. Each line type corresponds with the correct geometry, weight, and stiffness. All the lines were modelled as a 'Homogenous pipe', except for the Articulated Bend Restrictor (ABR), which will be modelled as 'General' to account for the nonlinear bend stiffness. Additionally, the general line type allows for an efficient way of experimenting with the length [41].
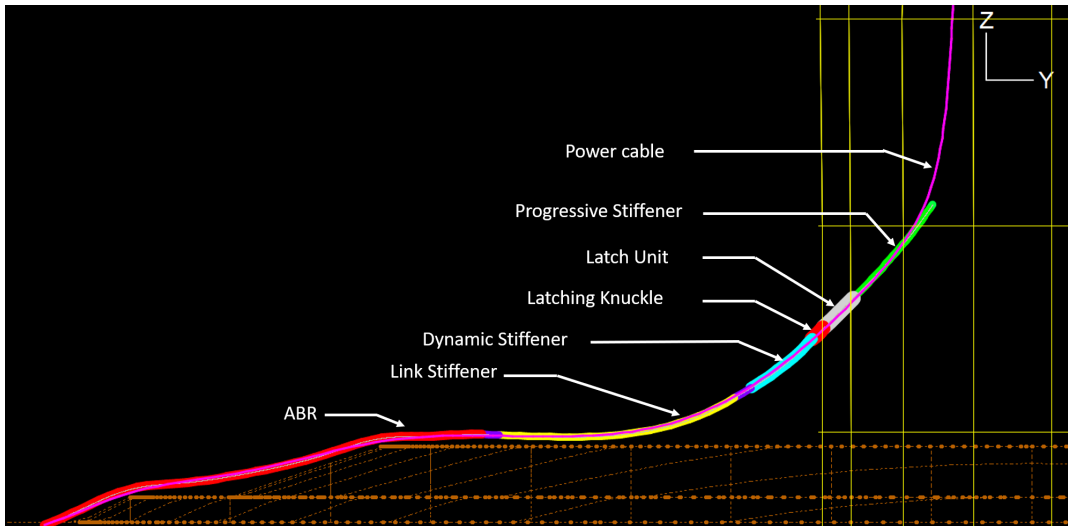
Figure 4.3: CPS Overview

The tip of the progressive stiffener is considered 'free', allowing it to hang free on the subsea cable. The other end of the CPS at the ABR section is buried into the seabed and therefore considered 'fixed'. At the location of the entry hole, a fixed 'buoy' is modelled. By using Mid-line connections, the CPS at the length of the latching unit is connected to this 'buoy', to ensure that the latching unit remains locked within the entry hole.

4.1.3. Power Cable Data

The cable model is configured as a line type. The selected subsea cable consists of three 300mm^2 conductors, which are suitable for the selected CPS [8]. The cable is given a bending stiffness (kNm^2), axial stiffness (kN), Poisson ratio and torsional stiffness (kNm^2). Furthermore, the cable has a maximum allowable tension and a minimum bend radius. The values are provided in Table 4.2. The different components within the power cable are explained in more detail in section A.1.

	Geometry	Structure					Limits	
	Outer Diameter (m)	Mass (kg/m)	Bending Stiffness (kNm2)	Axial Stiffness (MN)	Poisson ratio (-)	Torsional Stiffness (kNm2)	Allowable Tension (kN)	Minimum Bend Radius (m)
Cable 300mm2	0.1443	26	5.6	118	0.5	1.9	62.3	2.2

Table 4.2: Power Cable Properties

It is common practice to use a hang-off flange within a monopile to secure the power cable. Therefore, in the model, at the location of this hang-off flange, the cable is considered 'fixed'. The other end of the cable, although laying within the CPS, is also considered 'fixed'. Since most subsea cables are not designed for negative axial tension (compression), it is crucial to maintain tension throughout the entire length of the subsea cable. The tension helps to prevent the cable from kinking or bending. Furthermore, it assists in stabilizing the cable and remains in place [37].

4.1.4. Line Theory

As discussed the CPS and subsea cable are modelled as lines, each line is divided into straight massless segments with a node at each end. Each node is a short straight rod and represents the two halves of either side of the nodes, as shown in Figure 4.4. At the nodes, forces and moments are applied. The segments can be considered telescopic rods, which are connected by axial and torsion spring dampers [41]. In the CPS model, the segment length has been set to 0.2 meters. Consequently, this leads to 114 nodes at the CPS and 218 nodes for the cable.
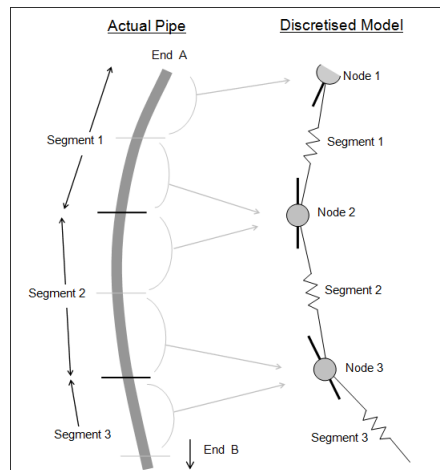
Figure 4.4: Line Theory [41]

4.1.5. Static Analysis

After all components are modelled and set up, a static analysis is performed. This determines the equilibrium position of the CPS and power cable under the internal loads such as weight, buoyancy and drag. Starting from the initial position, the equilibrium position is calculated by iterating until the net force is zero. The resultant equilibrium serves as the starting point for the dynamic analysis [41].

By iterative adjusting the length of the cable with both ends fixed, a cable length of 43.3 meters was found. Figure 4.5 shows the positioning from a top view of the static solved model. The static positioning of the system was inspected visually to confirm proper alignment of the cable and the CPS, with minimal curvature on the seabed, since excess curvature of the CPS would lead to a larger area that is exposed to the environmental loadings. In addition, the model is assumed to be symmetrical, as will be discussed in subsection 4.3.1. With a curved CPS on the seabed, this assumption would not be viable.

According to the guidelines in the DNV [37], compression in the cable should be avoided. Insufficient tension can result in a loop forming on the seabed and complicating the burial operations of the cable. In Figure 4.6, the tension range of the cable is shown. The orientation of the line in the graph is consistent with that of previous figures. This indicates that the left side aligns with the location of the buried cable, and the right side corresponds to the hang-off location.
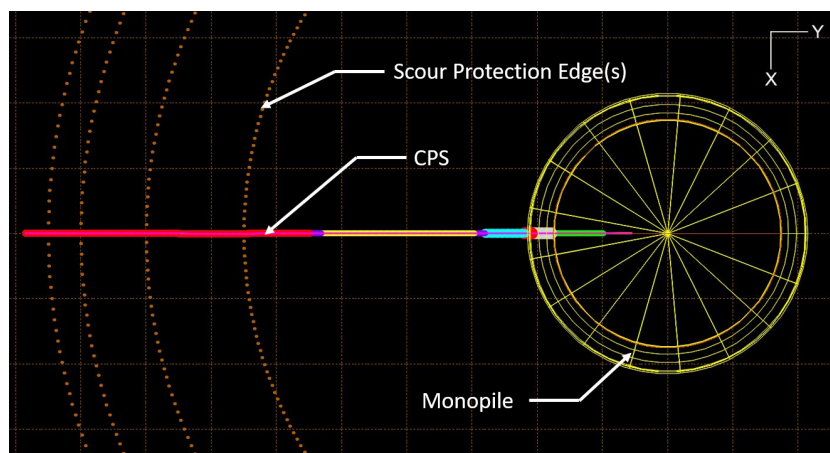
Figure 4.5: Static Topview

At the point of burial location, the power cable has a tension of around 2 kN. Following the tension of the power cable, it is shown that the tension increases. On the right part of the graph, the tension consistently rises due to carrying its own weight. Showing that there is no compression throughout the

entire length of the cable. In addition, the cable also remains far under the given maximum limit of 62.3 kN tension, which is typically only of concern during the installation phase [37].
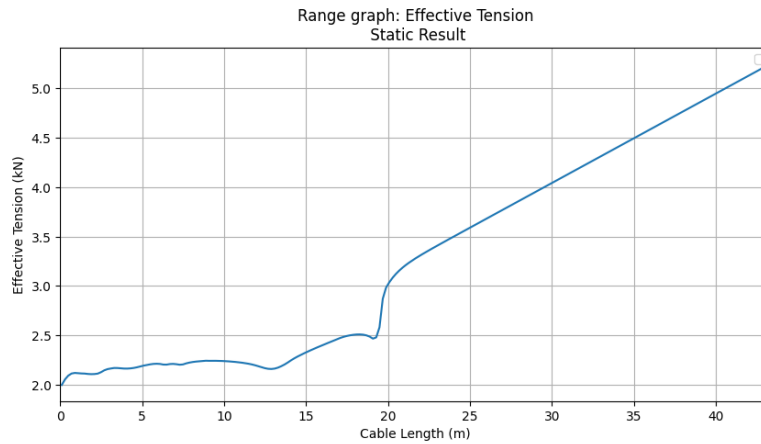
Figure 4.6: Cable Tension

Next, the bend radius of the cable was assessed to ensure it complies with the Minimum Bend Radius (MBR) requirements. Maintaining the cable's bend radius above the MBR is crucial because too overbending can lead to damage, such as insulation failure [44]. In Figure 4.7, the bend radius and the MBR are plotted. As shown in the figure, the cable bend radius is consistently higher than the MBR of the given 2.2m, as specified in Table 4.2. The extreme peaks in the cable's bend radius indicate that the cable is straight at these points.
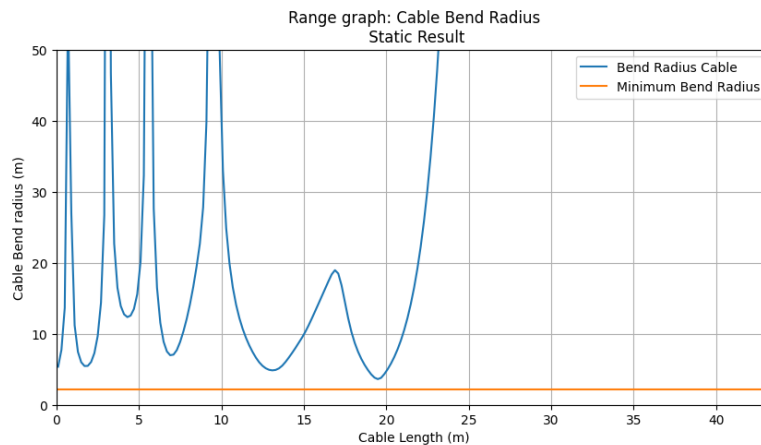
Figure 4.7: Cable Bend radius

4.2. Environmental data

Environmental data is incorporated into the model to conduct the dynamic analysis. This section will elaborate on the provided environmental data, which includes the water depth, wave and current speeds, directions and marine growth. Furthermore, it elaborates on how these parameters are applied and utilized within the system.

4.2.1. Location

For this study, the Gemini wind farm area is used. Gemini is located in the North Sea, approximately 67 km north of the coast. This wind farm consists of 150 wind turbines with a capacity of 4 MW, which leads to a total rated capacity of 600 MW. The site is separated into two areas, Zee-Energie (West) and Buitengaats (East), see Figure 4.8.

Figure 4.8: Gemini Location [45]

The Gemini location is assumed to be a suitable case study location since it has two offshore wind farms, which make use of a CPS, which has a similar set-up as the general setup of the CPS [46] as described in Appendix A.2. Since it is located in the North Sea, which is known for its harsh environmental conditions, testing the CPS in such conditions provides a realistic understanding of the challenges faced in the offshore industry. The MetOcean data was collected over 29 years (from January 1, 1979, to December 31, 2007). Extreme storms that occurred in 2006 and 2007 are therefore included in the hindcast data, which offer valuable information for the statistical extreme value analysis [35].

4.2.2. Water Depth
The reference point from which the wave data was obtained has a depth of 35.1 meters. Based on the MetOcean data [35] between 1979-2007 the maximum water levels are extracted and summarized in Table 4.3.

Water Level Parameter	Water level value (m MSL)	Water depth(m)
HSWL	2.20	37.30
HAT	1.15	36.25
MWL	0	35.1
LAT	-1.05	34.05
LSWL	-1.65	33.45

Table 4.3: Water Level

A water level lower than the Lowest Astronomical Tide (LAT) is possible due to a negative storm surge, which is caused by high atmospheric pressure. However, such a negative storm surge cannot coincide with an extreme storm. For this reason, the LAT will be taken as the lowest water level for the FLS, since it is assumed that a lower water depth, will lead to bigger loads on the CPS, considering the waves and current speed remain the same.

4.2.3. Wave Conditions
For the kinematics of the water flow, suitable wave data is employed to simulate the environmental conditions affecting the CPS. The MetOcean data is presented in a binned scatter table, shown in Table 4.4, which combines the significant wave heights and their peak period. The number represents the amount of occurrence of the sea state [47].

The hydrodynamic model uses the JONSWAP (Joint North Sea Wave Project) spectrum to simulate the waves. Based on North Sea measurements and observation in the North Sea, the JONSWAP spectrum accounts for sea states that are encountered within the North Sea, making it an appropriate spectrum for the hydrodynamic model. The peak enhancement factor of the JONSWAP spectrum is calculated

HS/Tp	<2	2	4	6	8	10	12	14	SUM
9	0	0	0	0	0	0	1	6	7
8	0	0	0	0	0	5	78	9	92
7	0	0	0	0	0	165	206	23	394
6	0	0	0	0	32	861	242	31	1166
5	0	0	0	0	617	2736	76	17	3446
4	0	0	0	24	6482	3758	38	20	10322
3	0	0	0	3430	19580	1840	65	25	24940
2	0	0	1053	34482	23762	2246	191	6	61740
1	0	329	47531	59386	20603	1425	31	0	129305
<1	3	2590	16220	3689	261	32	1	0	22796
SUM	3	2919	64804	101011	71337	13068	929	137	254208

Table 4.4: Binned Wave Scatter

using Equation 4.1.

$$
\gamma = \begin{cases} 5 & \text{for } \frac{T_p}{\sqrt{H_s}} \leq 3,6 \\ e^{\left(5,75-1,15\frac{T_p}{\sqrt{H_s}}\right)} & \text{for } 3,6 < \frac{T_p}{\sqrt{H_s}} \leq 5 \\ 1 & \text{for } 5 < \frac{T_p}{\sqrt{H_s}} \end{cases} \tag{4.1}
$$

As shown in Figure 4.9, the peak enhancement factor (γ) affects the distribution of the wave energy across the frequency (ω).
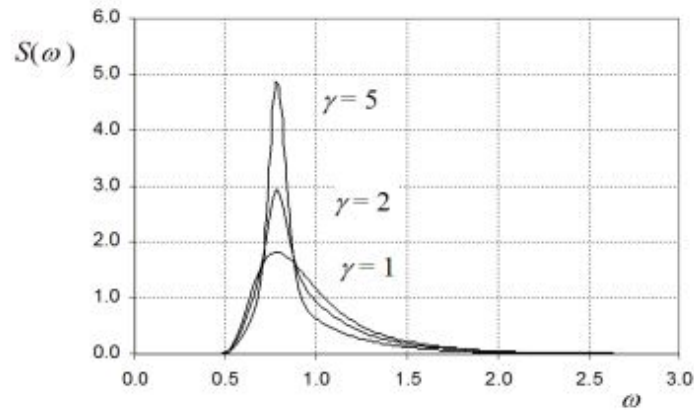
Figure 4.9: Peak shape [36]

Extreme Wave Conditions

Out of the MetOcean report [35], the peak values of the significant wave heights (H_{m0}) are extracted with their corresponding return periods. The significant wave height (H_{m0}) can then be used to calculate the peak period (Tp) and the maximum wave height (H_{max}) calculated, which are shown in Table 4.5. To obtain the peak period (Tp), Equation 4.2 & 4.3 are used.

$$
T_{02} = \gamma * (H_{m0})^{0.5} \tag{4.2}
$$

$$
T_p = 1.28 * T_{02} \tag{4.3}
$$

where: T_{02} = zero-crossing period
H_{m0} = significant wave height
γ = peakedness parameter
T_p = peak period

Assuming that the waves are Rayleigh-distributed, the maximum wave height is derived from Equation 4.4.

$$H_{max} = H_{m0} * (0.5 * \ln(t_{ref}/T_p))^{0.5} \tag{4.4}$$

where: t_{ref} = reference period (3h = 10800s)

Return Period (years)	$\mathbf{H_{m0}(m)}$	$\mathbf{T_p(s)}$
1	7.3	11.5
5	8.2	12.2
10	8.6	12.4
25	9.2	12.9
50	9.5	13.1
100	9.9	13.3

Table 4.5: Wave Return Periods

4.2.4. Current Conditions

In accordance with DNV [38], the current profile is modelled using the power law method (Equation 4.5). This method accounts for the relation between the current velocity and water depths [41].

$$U_c(z) = v_c(0) * \left(\frac{d+z}{d}\right)^{\alpha} \tag{4.5}$$

where: $U_c(z)$ = current velocity at level z
$v_c(0)$ = surface current speed
z = depth (negative number)
d = water depth
α = exponent – typically α=1/7

Extreme current speed

The following current speeds with their corresponding return periods were obtained from the MetOcean data [48]:

Return Period (years)	Velocity at Surface (m/s)
1	1.00
5	1.15
10	1.20
25	1.25
50	1.30
100	1.35

Table 4.6: Current Return Periods

The MetOcean report [48] provides a mean current velocity of 0.35 m/s at the surface. However, the presence of the monopile flow amplification has to be considered regarding the current velocity, as

suggested by a recent report [17]. The currents need to travel around the monopile, which can lead to significantly higher dynamic velocities than were initially considered.

To account for the current flow amplification, a current velocity significantly higher than the current mean velocity has been selected. The selected value current velocity is 1.00 m/s, corresponding to a return period of once a year. In the simulations, the current direction is assumed to be co-linear with the wave direction. This assumption, which prevents the environmental loadings from cancelling each other, is considered to be the most unfavourable and, therefore, conservative.

4.2.5. Marine Growth

Submerged structural components are often subjected to marine growth, which can have a significant influence on the behaviour of the components due to the increased dimensions and roughness. Marine growth is site-specific. However, no local marine growth data was found. Therefore, DNV [39] was used to estimate the marine growth thickness. The obtained values are shown in Table 4.7. For the parts of the CPS lying on the seabed a marine growth of 50% is applied, as contact with the seabed will prevent the development of marine growth and the movement between the seabed and the CPS will tend to remove developed marine growth.

Parameter	Thickness (mm)	Density (kg/m^3)
Free span CPS	100	1325
Bottom Touching	50	1325

Table 4.7: Parameters for marine growth

4.2.6. Hydrodynamic Loads

The model calculates the hydrodynamic loads using an extended version of Morison's equation, see Equation 4.6. The Morison equation consists of two components: fluid inertia force and drag force.

$$f = \underbrace{C_{\mathrm{m}} \Delta a_{\mathrm{f}}}_{\text{inertia}} + \underbrace{\frac{1}{2} \rho C_{\mathrm{d}} A \left| \boldsymbol{v}_{\mathrm{f}} \right| \boldsymbol{v}_{\mathrm{f}}}_{\text{drag}} \tag{4.6}$$

where: f = fluid force (per unit length) on the body
C_{m} = inertia coefficient
Δ = the mass of displaced fluid
a_f = fluid acceleration
ρ = density of the water
C_{d} = drag coefficient
A = drag area
v_{f} = fluid velocity

Using DNV [36], a conservative maximum inertia coefficient (C_M) value of 2 is adopted. The inertia coefficient (C_M) is defined to be equal to $1 + (C_A)$ therefore the (C_A) is set to 1.0. Resulting in an inertia coefficient of 2.0.

The drag coefficient is based on the Reynolds number. The Reynolds number is a dimensionless quantity that helps to determine whether the fluid flow is laminar or turbulent state. To find the correct drag coefficient, the hydrodynamic model calculates the Reynolds number using Equation 4.7

$$Re = \frac{vl}{\nu} \tag{4.7}$$

where: Re = Reynolds Number
v = velocity
l = length
ν = kinematic viscosity of the fluid

The correlation between the Reynolds number (Re) and the drag coefficient (C_D) is based on a rough riser, as suggested by [49]. This rough riser has k/D ratio of 1.0 x 10^{-3}. According to the DNV [36], this results in the following graph, which functions as the input value for the hydrodynamic model to calculate the drag coefficient.
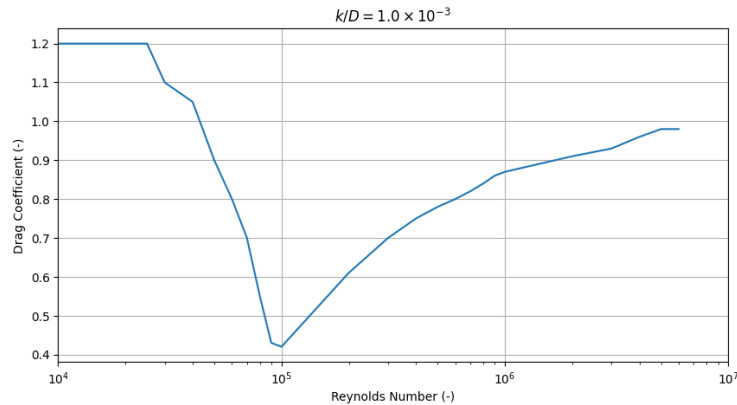
Figure 4.10: Reynolds Number vs Drag Coefficient

4.3. Dynamic Analysis

After the static analysis and the discussed environmental data were implemented, the dynamic analysis was performed. This allows for obtaining the response of the system and its behaviour during time-varying loads. There are two methods to perform this dynamic analysis: frequency domain and time domain [41]. The frequency domain is a linear analysis; the non-linearities are approximated by linearization. Frequency domain analysis is often more efficient than time domain analysis. However, due to its linearity and time invariance, it has limited applicability. More critically, fatigue calculations are predicated on historic loading cycles, making frequency domain analysis unsuitable for determining fatigue life.

Therefore, a time domain analysis is used. The time domain analysis is completely nonlinear, with the mass, damping, stiffness and loading evaluated at each time step [41].

4.3.1. Fatigue Limit State Simulation Cases

For the fatigue limit state calculation, different combinations of the wave height, peak period and directions are assessed. These are shown in Table 4.8.

Parameter	Value	Amount of values
Wave and Current Direction (deg)	90, 120, 150, 180, 210, 240 270	7
Significant Wave height (m)	2, 3, 4, 5, 6, 7, 8, 9	8
Peak Period (s)	4, 6, 8, 10, 12, 14	6

Table 4.8: FLS input cases

The variation of value at the three parameters resulted in a total of 336 unique combinations. These combinations were simulated for 3 hours, as suggested by DNV [36]. As illustrated in Table 4.8, the assessed directions ranged from 90 to 270 degrees. The black coordinate system within the figure corresponds with the global coordinate system. Given the symmetry of the hydrodynamic model, shown in Figure 4.11, no difference in results between the symmetrical direction is assumed. Meaning that the direction of 300° corresponds with the direction of 240°. Similarly equivalence between the directions: 210° with 330°, 180° with 0°, 150° with 30°, and 120° with 60° are assumed. By simulating for only 7 instead of all 12 directions 270 simulation cases are excluded.

To reduce the computational time, the wave scatter diagram shown in Table 4.4 has been compressed

(binned). Additionally, the waves with a significant wave height lower than 0.5 meters or waves with a peak period of less than 2.5 seconds have been excluded, as they are not expected to have a significant effect on the the CPS.
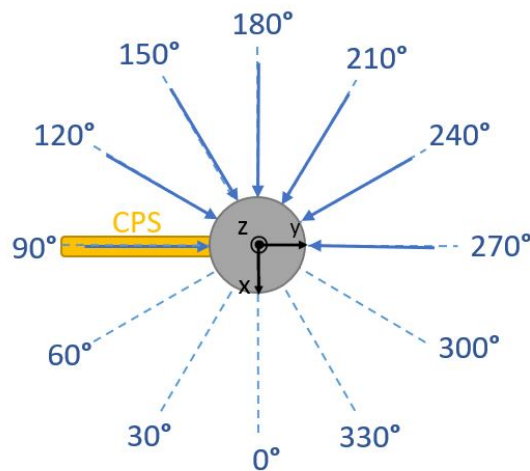
Figure 4.11: Direction Overview

4.4. Dynamic Results

After the dynamic analysis has been completed, the forces and moments for each node on the CPS are calculated. These data points, illustrated in Figure 4.12, represent the forces and moments based on the expected most extreme sea conditions, which corresponds to the highest wave height and longest peak period, in a perpendicular direction of the CPS, with parameters; 9 meters, 14 seconds and 180°.

The representation of the minimum and maximum calculated shear forces and bending moments that are obtained over the entire 3-hour simulation on the length of the CPS. Consistent with the other figures, the left side of the graph denotes the burial location, and the right indicates the location of the monopile. The graphs enable the identification of the greatest load fluctuation, which is considered important since large stress fluctuations are expected at locations with greater loading variability.

As shown in the figures, there is a significant load fluctuation observed as the CPS transitions into the monopile, which is also suggested by Felici [4]. These relatively large bending moments are expected since the latched part is considered fixed. Therefore, it offers significant resistance to these bending forces. Resulting in higher bending moments close to the fixed latching unit.

A comparison between the location of the high fluctuation and the corresponding components of the CPS shows an overlap with the CPS knuckle. This overlap is represented within the graph by the two additional red lines, representing the start and end location of the knuckle.

Despite that the CPS is designed to withstand these high moments and shear forces at this location, industry experience [6] has shown that failure close to the entry hole is not uncommon. Considering these insights, the focus regarding the failure of bolts has been narrowed to the knuckle area.

4.4.1. Loading Results

The loading results, which will be applied to the structural model, are obtained from node 32 of the CPS line within the hydrodynamic model. This particular node represents the location of the end of the latching knuckle and the start of the dynamic stiffener, as illustrated in Figure 4.13a. The figure shows the local axis on node 32, where the Z direction follows the CPS towards the point of burial. The local coordinate system is right-handed, meaning that positive moments are clockwise when looking in the direction of the axis, and positive shear is in the direction of the axis system.

(a) x-shear

(b) y-shear

(c) x-bend moment

(d) y-bend moment
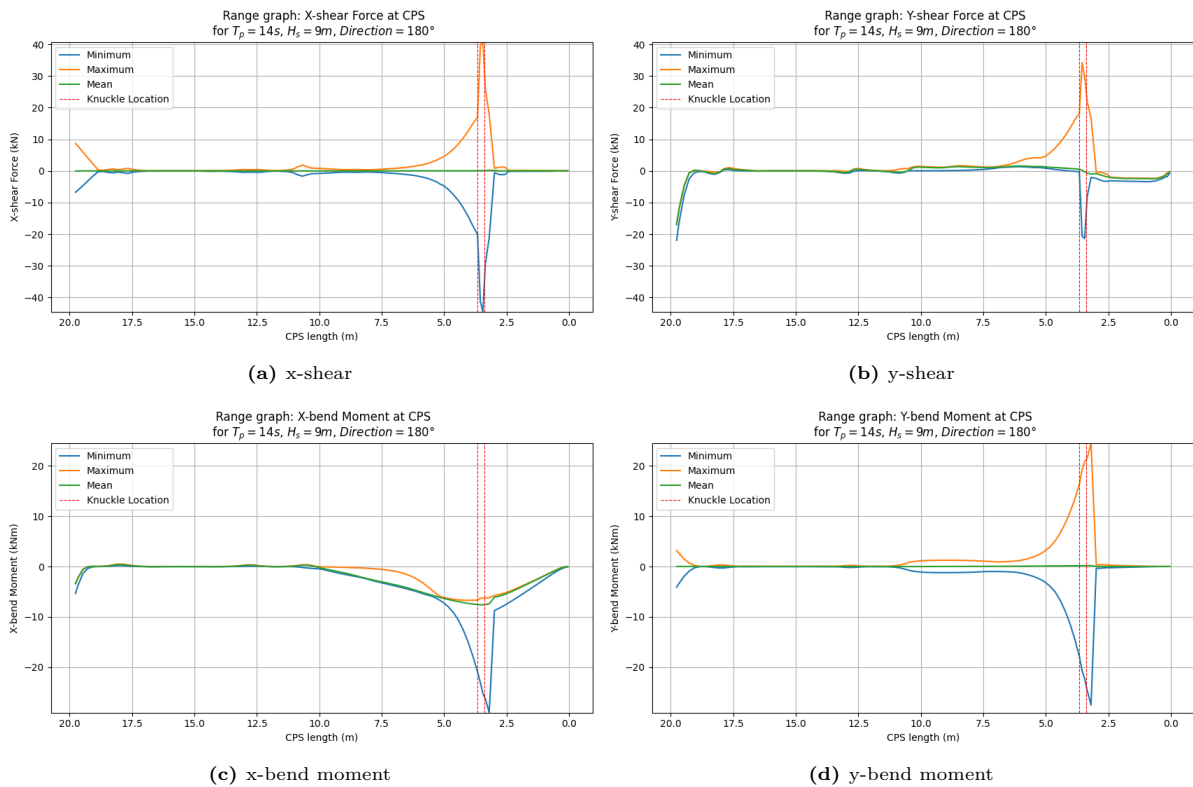
Figure 4.12: Moments and Shear forces at the CPS

Figure 4.13 illustrates the five loading results in the time domain in the most severe case.

4.4.2. Movement
During the high sea-states simulations, the CPS moves heavily across the scour protection, as illustrated in Figure 4.14, where the grey area represents the envelope of the CPS movements.

To get a better visualize of the movement of the CPS across the scour protection, the velocity at node 75 has been plotted in Figure 4.15.

4.4.3. Loading peak analysis
When comparing the loading results of Figure 4.13 with Figure 4.15, particularly the peaks of the graphs, it becomes evident that the loads obtained correspond with the movement of the CPS. This confirms that by mitigating these relatively large movements of the CPS, lower load fluctuations will occur. In practice, additional rocks or rock bags are installed to prevent movement of the CPS [50]. However, according to the recent report [17], the impact of these rocks on top of the scour protection could have an impact on the deformation of the scour protection. Moreover, when installing these rocks on the CPS, it is crucial to be aware of the impact energy.
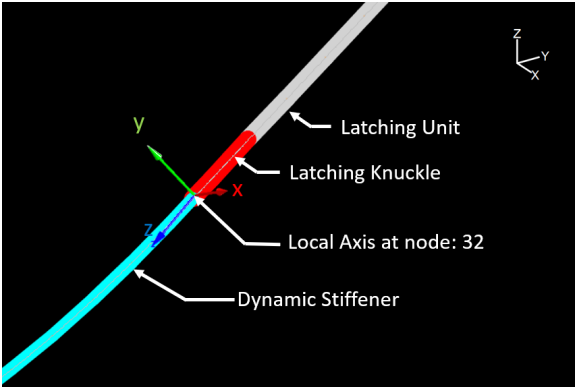
(a) Local Axis system at node 32
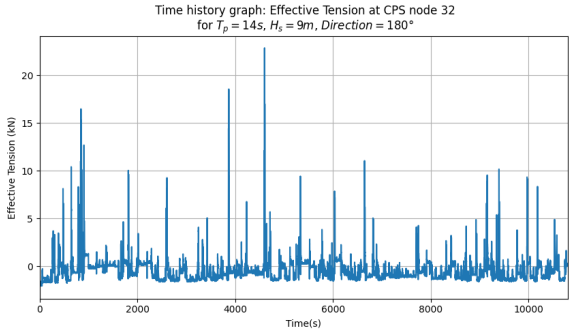
(b) Tension (kN)
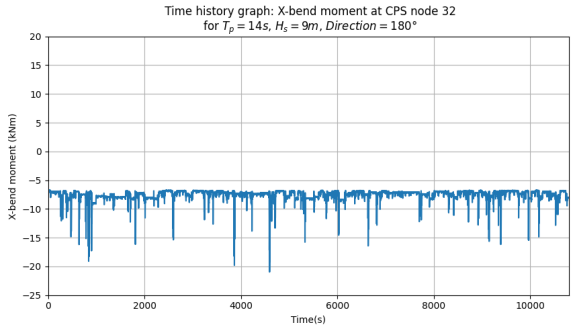
(c) X-bend moment (kNm)
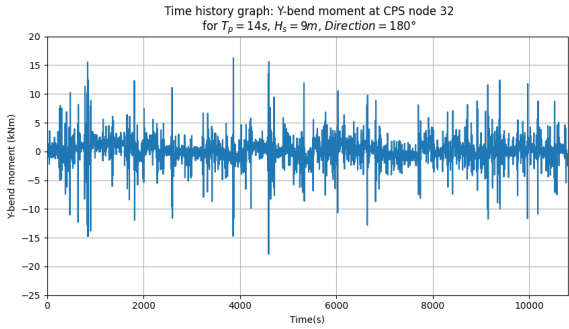
(d) Y-bend moment (kNm)
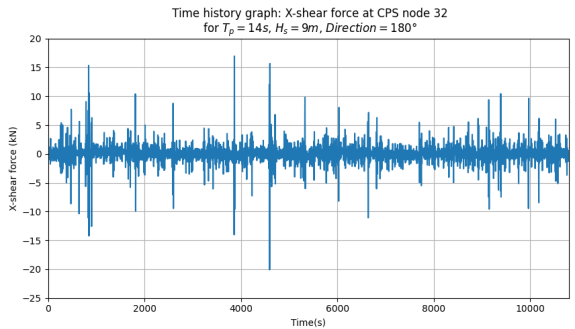
(e) X-shear (kN)
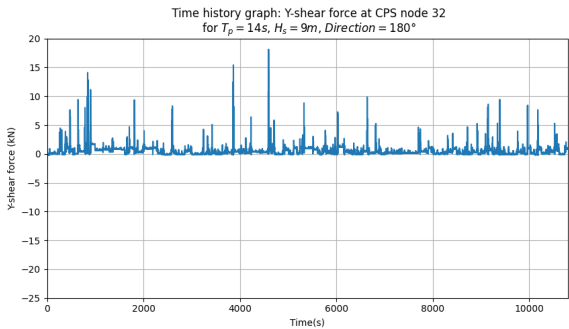
(f) Y-shear (kN)

Figure 4.13: Loading Results in Time Domain
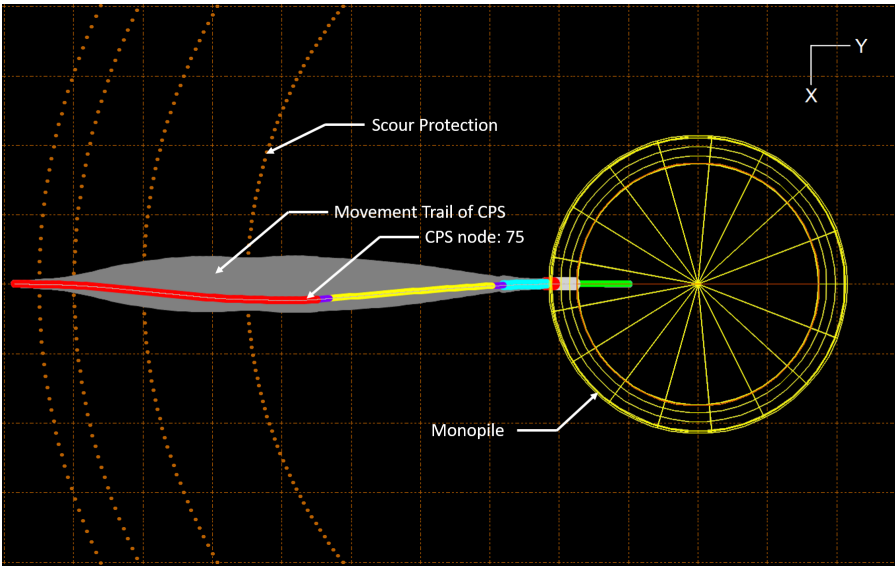
Figure 4.14: Envelope of the movements
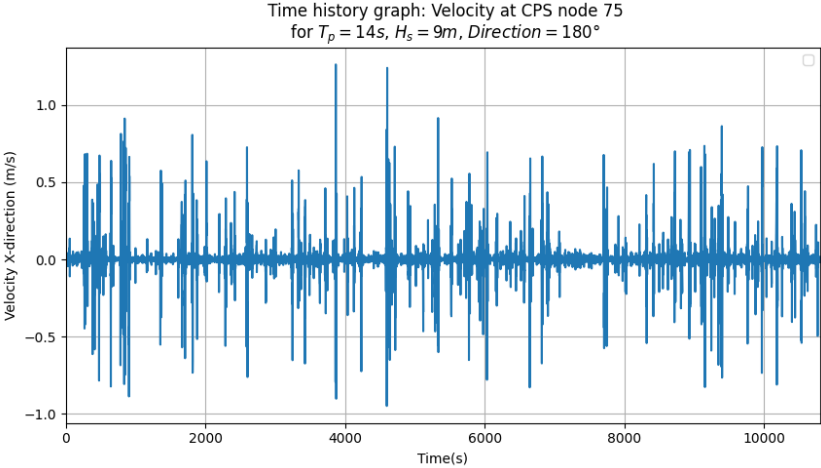
Figure 4.15: Velocity X-direction (m/s) at node 75

5

Structural Analysis

A FEM model of the susceptible section of the CPS is developed. A FEM is a technique for formulating and solving a system of equations. The main reason for using a FEM model is the ability to solve arbitrarily complex problems that would be too time-consuming and complex to solve by hand [51]. The structural model was developed using the commercial FEM software Ansys. The software includes a full complement of linear and non-linear elements, material laws and a wide range of solvers. It can handle complex assemblies and is useful for determining stresses, displacements and contact pressure distributions on the assembly. These capabilities make it suitable for assessing the bolts.

5.1. Setup

The development of the structural model is divided into five main steps:

1. **Geometry:** Specifying the dimensions of the structure.
2. **Material Properties:** Assigning the relevant material characteristics.
3. **Contact Regions:** Identifying possible interaction between components.
4. **Mesh:** Dividing the structure into finite elements.
5. **Constraints:** Apply the boundary conditions.

5.1.1. Geometry

The development of the structural model begins with defining its geometry. This section provides an overview of the geometry used in the structural model, with an explanation of the CPS components followed by the geometry of the bolts.

Section Components

Based on the experience from the industry and the calculated extreme loads located at the latching knuckle, shown at Figure 4.12, the bolts within the knuckle are considered the points of interest for this research. These bolts secure both halves of the knuckle together. In Figure 5.1, the components of CPS are shown disassembled. Within the figure, the latching unit, upper and lower knuckle, the dynamic stiffener and the bolts to connect the upper and lower knuckle are visible.

After assembling the CPS components, the system appears as Figure 5.2a. The original coordinate system of the hydrodynamic model was not the same as that of the structural model. An additional coordinate system was created to ensure consistency. This coordinate system is shown at the end of the knuckle in Figure 5.2a. This coordinate system mirrors the coordinates system of the hydrodynamic model at node 32, as shown in Figure 4.13a. This allows for the direct input of the hydrodynamic load results in the structural model. The connected knuckle parts geometrically clamp the latching unit and the dynamic stiffener together, as is illustrated in Figure 5.2b.

The latching knuckle connects the main body of the latching unit and the dynamic stiffener. Due to the clamping, the forces and resistance on these sections could impact the force distribution, consequently

impacting the bolt loads. Therefore, both the dynamic stiffener and latching unit are included within the model.

Since only the clamped part of the dynamic stiffener is of interest, it has been partially cut. Likewise, the locked geometry of the latching unit is modelled accurately, while the remaining geometry is less detailed to avoid additional computational time.

The latching unit is assumed to be securely locked with the monopile. Since the monopile will function as the location for the constraints, explained in subsection 5.1.5, it is also included in the model. However, as this is not considered the area of interest, the monopile is only partially modelled.
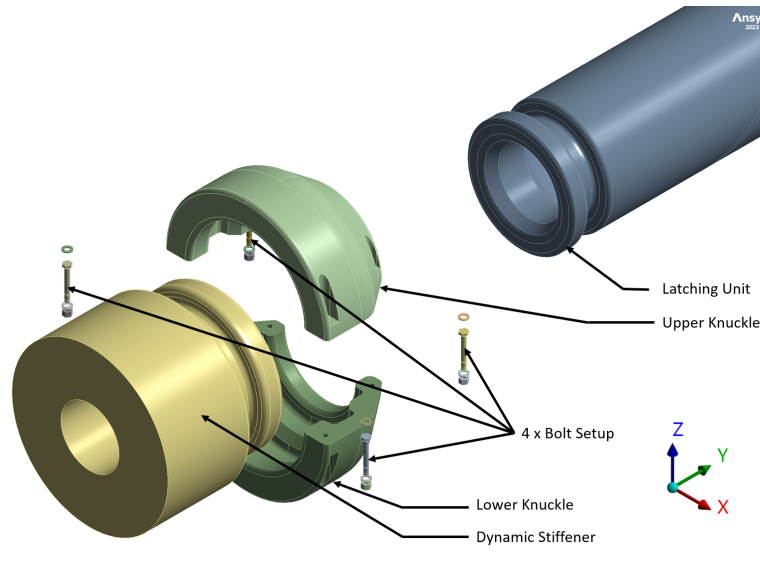
Figure 5.1: Disassembled CPS components

(a) Side View of the CPS

(b) Cross-Sectional Side View of the CPS
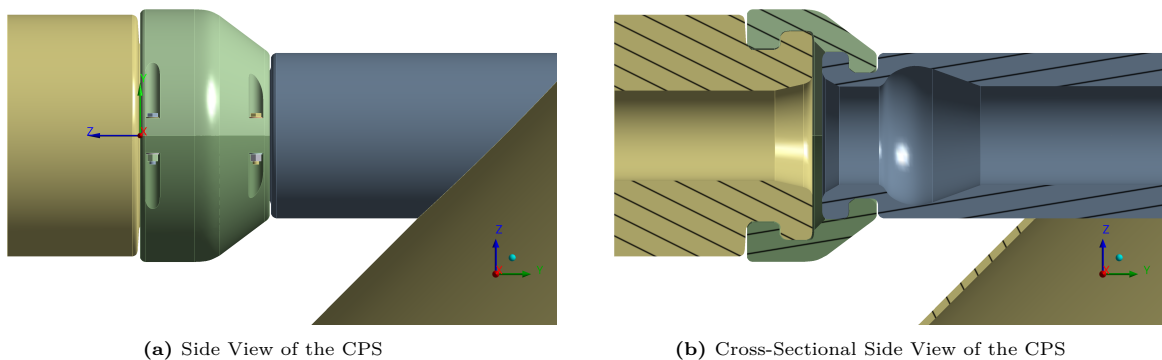
Figure 5.2: CPS section overview

Bolt Assembly

In the generic CPS model, a DIN 931 M16 galvanised bolt has been used, together with a DIN 125-1A galvanised M16 plain washer and a fitting DIN934 galvanised M16 Nut. The term 'DIN' refers to the German Institute for Standardization (Deutsches Institut für Normung). DIN standards are well-recognized and used in many industries.

There are numerous ways to model a bolted joint, as presented in Appendix B. These bolt models vary in precision, computational time and memory usage. The most accurate solid bolt model has a real thread, and the dimensions of the head and nut are also accurate. The simplest model shows a beam connection between the two flanges without representing the bolt.
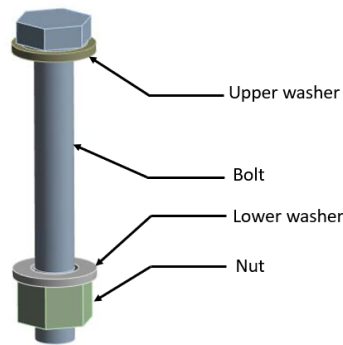
Figure 5.3: Bolt Assembly Geometry

It is important to note that only solid elements can capture the stress and shear in the bolt head, nut and local stresses in threads [52]. Furthermore, modelling friction between different parts requires the parts to be modelled as solids. Therefore, this model uses only solid elements. Since the bolt head and nut geometry could impact the stress distribution, the head and nut will be modelled accurately instead of being modelled as a cylinder. Figure 5.3 shows the geometry of the bolt setup, which includes the bolt, washers and nut. The specific dimensions of the bolt assembly are detailed in Appendix C.

To visualise the peak stresses within the thread without drastically increasing the number of nodes at the bolt, the thread is defined in the options of contact. This method is referred to as Geometric Correction [53]. When looking at Appendix B, the chosen model represents the second from the top, referred to as the "Bolt model with thread defined in options of contact".

5.1.2. Materials
Designing the right properties is essential for the model. The materials are chosen based on recent CPS design [8]. The latch body and latch knuckle are made from cast iron. The dynamic stiffener in the design is made from polyurethane. Since polyurethane can be adapted to provide the required flexibility to transfer the load. The monopile is made out of S355 steel.

Regarding the bolt assembly, all the bodies are made out of stainless steel with grade 8.8. Class 8.8 is often used for offshore structures. In these classes, the first number represents the minimum specified tensile strength of the bolt in MPa multiplied by a hundred. The second number, including the dot, represents the minimum specified yield strength to tensile strength. Consequently, a property class of 8.8 can be interpreted as the minimum tensile strength of 800 MPa and 800 * 0.8 = 640 MPa yield strength [29]. Based on the ultimate limit strength, the proof load can also be calculated. The proof load defines the maximum tensile force that can be applied to a bolt that will not result in plastic deformation. Therefore, often 90% of the yield strength is taken [9]. This results in a proof load of 800*0.9*157 = 90.43 kN.

One reason that class 8.8 bolts are commonly used within the offshore industry instead of higher strength classes, like 10.9 or 12.9, is to prevent Hydrogen Induced Stress Cracking (HISC). According to DNV [54], a maximum of 350 Hardness is required to prevent HISC. In ISO code [55], it is shown that higher strength classes exceed this hardness value, making them less suitable for preventing HISC.

In addition, all bodies of the bolt assembly are galvanised. This zinc coding provides additional protection against corrosion, which is useful for subsea use. However, this coding negatively impacts the fatigue strength [56]. The zinc coding on the galvanised bolts can attract hydrogen atoms, and this absorbed hydrogen increases the possibility of stress cracking within the bolt, thereby reducing its fatigue resistance.

In the structural model, in line with DNV [57], a linear-elastic material is used for the bolt assembly. The elastic material properties include the Poisson's ratio and the Young's Modulus. The material properties for each component applied within the structural model are shown in Table 5.1.

A linear-elastic material has some limitations since it does not account for the strain-hardening effect. Many metals, including the stainless used for the bolts, are subjected to a phenomenon known as strain
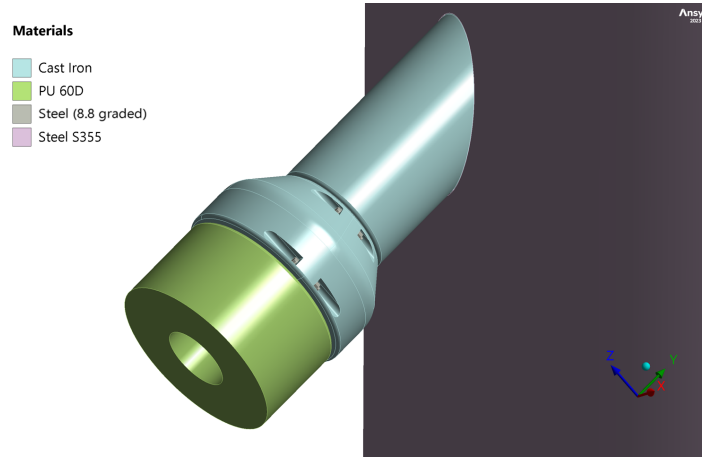
Figure 5.4: Material Assignment

Component	Material	Young's Modulus (MPa)	Poisson's Ratio (-)	Yield Limit (MPa)	Ultimate Limit (MPa)
Monopile	S355	2.05E+05	0.27	355	490
Latch Body	Cast Iron	1.76E+05	0.275	273	408
Latch Knuckle	Cast Iron	1.76E+05	0.275	273	408
Dynamic Stiffener	PU 60D	86	0.5	-	56
Bolt Assembly	Steel (8.8 Graded)	200E+03	0.3	640	800

Table 5.1: Material Properties [8]

hardening. When the material deforms, when it exceeds the yield strength, it often becomes stronger and more resistant to further deformation [58]. This is typically relevant for the first thread in the bolt, as shown later. However, since the fatigue calculations are based on the nominal stress of the bolt, these local effects are not considered crucial.

5.1.3. Contacts

The contact regions are defined to describe the interaction between the bodies. When the bodies come into contact, forces are exerted, allowing them to detect each other. The objective of the contact formulation is to determine how these pressure forces are distributed.

There are different contact types to model the contact between contact regions. Careful judgement is made about where and what kind of (non)linear contact is needed. In essence, the force vector acting at contact can be resolved in a normal force (F_n) and a tangential force (F_t) at the contact point. In the model, only bonded contact and frictional contact are defined.

Bonded contact does not allow for sliding or separation. The contacts can be considered as if they were glued together. The normal force (F_n) and a tangential force (F_t) are so strong (see Equation 5.1 and Equation 5.2) that no relative motion can occur. This constraint allows for a linear solution. In reality, however, such contacts do not exist, but they are considered helpful when applied correctly.

$$F_n \longrightarrow \infty \tag{5.1}$$

$$F_t \longrightarrow \infty \tag{5.2}$$

In the model, it is assumed that the latching unit is latched secured in the monopile and does not allow for movement. Therefore, this contact has been considered bonded. In reality, this part is geometrically clammed, but since the model is focused on the bolts, which are relatively far away from this latching area, no difference is assumed in the result.

All the other contacts, including the various clamped CPS sections and the bolt contacts, are all modelled with non-linear frictional contact. The model uses Normal Coulomb's law of friction Equation 5.4, which states that the friction force is proportional to the normal force.

$$F_n = \begin{cases} 0, & \text{away from the surface} \\ F_n, & \text{into the surface} \end{cases} \tag{5.3}$$

$$F_t = \mu F_n \tag{5.4}$$

For each individual bolt assembly, there are eight contacts considered:

1. Contact between the bolt head and the (upper)washer

2. Contact between the (upper)washer and the (upper)knuckle

3. Contact between the (lower)washer and the (lower)knuckle

4. Contact between the nut and the (lower)washer

5. Contact between the bolt shaft and the (upper)washer

6. Contact between the bolt thread and the (lower) washer

7. Contact between the bolt shaft and the upper and lower knuckle

8. Contact between the bolt thread and the nut

Friction Coefficient
Based on DNV [40], a friction coefficient of 0.20 is assumed between the different sections of the CPS. Regarding the bolt friction, a similar friction coefficient of 0.20 was used, following DNV [57]. This value corresponds with laboratory tests conducted by TNO [59], which determined a friction coefficient within the range of 0.14 and 0.24 between coated steel surfaces within seawater.

Symmetry of Contact
A contact pair can be symmetric or asymmetric. Similar to DNV [57], an asymmetric contact behaviour is assumed. Asymmetric contact defines one surface as 'slave' and the other surface as 'master'. As for symmetric contact, both surfaces function as 'slave' and 'master' simultaneously. The defined 'slave' surfaces are not capable of penetrating the 'master' surface. As recommended, the used model defines the more finely meshed as a 'slave' surface. Since the model uses a finer mesh for the bolts, these are defined as 'slave' surfaces.

5.1.4. Meshing
After the geometry has been imported and the contacts are assigned, a meshing is performed. A mesh consists of elements which contain nodes. That way, they represent the shape of the geometry. It plays an important role in the accuracy of the simulation results. Finer meshing generally provides more accurate results. However, a finer mesh also leads to an increase in elements, simulation costs, and running time. Maintaining a balance between the mesh size and the precision is crucial. Not only is the mesh size significant, but the meshing method also contributes to the meshing procedure. Several meshing methods are available: tetrahedral element meshing, hexahedral element meshing, automatic method, sweep meshing and hybrid meshing.

The first two (tetrahedral and hexahedral) are the most commonly used meshing methods. For the model, an initial automatic coarse mesh was created, followed by manual adjustments. Although hex elements are often considered more accurate, the complexity of the designed segments led to tet elements as a better fit for this model, as shown in Figure 5.5. Additionally, contacts were manually meshed due to their importance. Since the material can be impacted by other parts of the contact.

Since this study is focused on the bolts, detailed meshing was applied to the bolts, as shown in Figure 5.6. A hybrid meshing technique called Multi-zone was used for the bolt. This Multi-zone method uses a combination of hex and tet elements [60]. It applies the more accurate hex elements that it is applicable

to and uses tet elements where it can not apply these hex elements. Furthermore, the nut and the washer are meshed using this method.
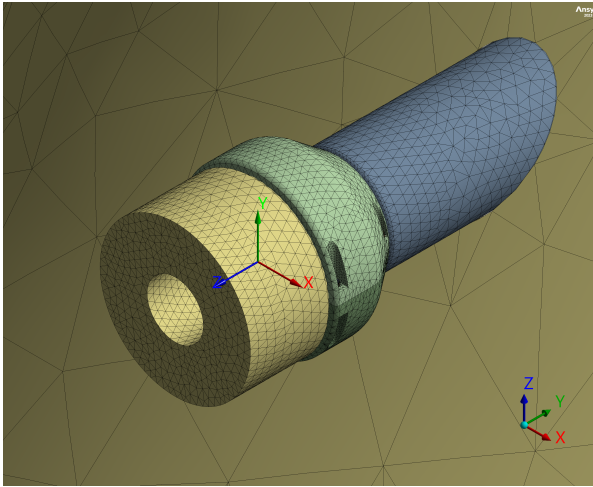
Figure 5.5: CPS mesh
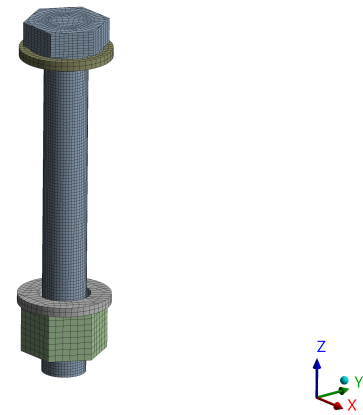
Figure 5.6: Bolt Mesh

5.1.5. Constraints

Constraints in the model function as boundary conditions and prevent undesirable rigid body motion. In the model, the monopile is considered to be rigid. This is done by applying two constraints, as shown in Figure 5.8. The monopile area, which is buried in the seabed, functions as a fixed support, which simulates the immobility due to the seabed. Secondly, the edges of the monopile have a remote displacement of 0 for all three directions (x, y, z). However, the remote displacement does allow for rotations.

The constraints may be excessive, but the impact on the required results is negligible because no deformation is expected. Also, the deformation of the monopile is not the point of interest and only functions as a rigid body for the CPS within the system. The model assumes that the CPS is securely latched into this fixed monopile. Meaning that the latching unit component is free to deform but remains fixed at the point of latching.
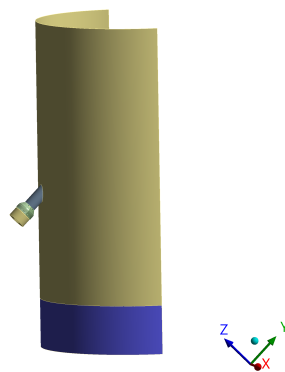
Figure 5.7: Applied Constraints
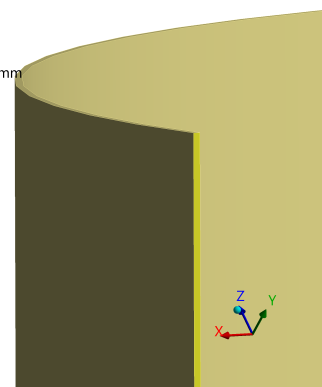
Figure 5.8: Applied Constraints

5.2. Loading Model

Once the model is set up, the loadings will be applied. This section will detail the process of how the model is loaded.

5.2.1. Safety and Load Factors

Table 5.2, extracted from DNV [39], provides guidance on the appropriate application of load factors for both the ULS as well as the FLS.

Functional and Environmental Loads			Permanent Loads*		
ULS		FLS	ULS		FLS
Normal**	Abnormal***		Favourable	Unfavourable	
1.35	1.1	1.0	0.9	1.1	1.0

Table 5.2: Load Factors

* Permanent load is defined as the total weight minus the buoyancy, determined at the still water level.
** The normal load factor for the ULS is the expected routine occurring loads on a structure and can be considered standard operation conditions.
*** The abnormal load factor is applied to loads that are less frequent but could still occur during the lifespan of the structure. Events like extreme weather can be considered an abnormal load factor.

As can be seen in the table, the FLS has a load factor of 1.0 for both the permanent load and the environmental load. While the load factor 1.0 can be assumed, DNV [61] states that fatigue damage accumulates through all phases. Therefore, it suggests considering the highest safety factor when accumulating the fatigue damage. As a result, a Design Fatigue Factor (DFF) of 10.0 should be applied.

5.2.2. Bolt Preload

The first loading step in the structural model is preloading the bolts. In reality, torque is applied, which rotates the bolt when installed. In that way, the bolt grip length is reduced, resulting in a tensile preload [29]. However, when modelling bolts within the structural model, it is not necessary to model the torque, which leads to thread insertion. In fact, excluding this is preferred since it adds no accuracy and increases the computational costs.

Instead, within the model, the bolts are split into two parts. On each half of the cylinder, nodes are picked. These nodes need to be physically coincident. By applying relative displacement or a specified preload force on the two nodes, the tensile force is simulated. This approach is generally used to shorten the grip lengths of the bolt. This preload step is the first loading step when applying force. To keep these adjustments constant when applying other loading factors, the bolts are 'locked'. Since the bolts are loaded prior to the other loads, the model is considered a "multi-step model" [62].

The amount of preload applied to the bolt is often calculated by a percentage of the allowable yield stress of the bolt. This percentage is not always the same, R. Budynas and K. Nisbett [9] suggests using 77% of the bolt yield stress, for example. In the model, the applied preload is based on DNV [40]. This suggests that 70% of the bolt yield stress should be applied to reduce the possible fatigue damage. The preload is calculated using Equation 5.5.

$$F_{PL} := \%_{yld} * S_{ty} * A_{tensile} \tag{5.5}$$

where: $\%_{yld}$ = The fastener allowable utilisation of yield strength (0.70)
S_{ty} = Grade 8.8 has an allowable stress yield (640.0 MPa)
A_t = The tensile bolt area (157 mm^2)

Equation 5.5 results in a bolted preload (F_{PL}) of 70.34 kN. When applying this preload, a tensile mean stress of 448.75 MPa is obtained at the bolts. This tensile mean stress is similar to the expected stress

when calculating the tensile stress by hand using Equation 5.6

$$\sigma_{PL} := \frac{F_{PL}}{A_t} = 448.02\text{MPa} \tag{5.6}$$

Bolts can loosen over time due to the cyclic loading and the vibration. According to R. Budynas and K. Nisbett [9], this can be prevented using enough preload. They suggest that a preload of 60% of the proof load rarely leads to self-loosening bolts. Given that the bolt within the model has a proof load of 94 kN and the applied preload is 70.34 kN, it is well over 60%, and the risk of self-loosening of the bolts is reduced.

5.2.3. Loading cases
The fatigue assessment, which will be elaborated upon in section 6.1, will utilize the nominal stress approach for calculations. This approach employs the tensile stress in the cross-section of the bolt [63]. Given that the bolt cross-section is known, the fluctuations in stress originate from the forces within the bolt.

With the structural model, the bolt tool was utilized, which evaluates all forces acting through the pretension cut, referred to as 'workload' [27]. This tool is employed to determine the nominal stress for the bolts.

The extreme values (minimum and maximum) are incorporated into the structural model. Since these extreme values do not occur alone. The corresponding loads obtained from the hydrodynamic model simultaneously are also included within the model, similar to Table 5.3. The aim is to establish a correlation and to achieve this, the model's quality is enhanced by increasing the number of data points. Therefore, a large number of corresponding loadings, captured at random moments from the hydrodynamic model, are also included.

5.3. Loading Steps
As explained previously, first the preload was applied to the bolts, this was done in the first step. Afterwards, the bolts were 'locked', as suggested by DNV [40]. Afterwards, the loadings, shown in Table 5.3, were applied to the structural model. These values are applied directly from the coordinate system since this mirrors node 32 of the hydrodynamic model, from which the results were obtained. The applied moments and forces are based on the highest values obtained in the hydrodynamic model for the most severe sea state. For a fatigue calculation, the load factor remains 1.0, as shown in Table 5.2. The obtained load results from OrcaFlex can, therefore, be directly applied to the model. In this example, the loading result at 4596.8 seconds is taken from the same case illustrated in Figure 4.13.

Step:	Bolt Preload (kN)	Shear/Tension (kN)			Moment (kNm)	
		x	y	z	x	y
1	70.340	0	0	0	0	0
2	'locked'	-5.017	4.487	5.711	-5.208	-4.463
3	'locked'	-10.035	8.975	11.423	-10.416	-8.926
4	'locked'	-15.053	13.462	17.134	-15.624	-13.39
5	'locked'	-20.070	17.949	22.845	-20.832	-17.853

Table 5.3: Loading Steps

For the fatigue calculation, an estimation is needed to calculate the working load and, thereby, the stress within the bolts. Therefore, the results of all the sea states are assessed with the extreme (minimum and maximum). Since these extreme values do not act alone on the CPS, the corresponding other loads are obtained from the OrcaFlex simulation results.

In Figure 5.9, the four preloads (A, B, C, D) at each bolt are shown. These are illustrated by the arrows pointing towards each other. The x and y moments are combined and are represented by the yellow curved arrow (E), and the x and y shear and tensile force are combined and visualized by the straight

blue arrow (F). This resulted in shear and tension from Table 5.3, resulting in a force of 35.311 kN, similar to a resultant moment of 27.435 kNm was found.
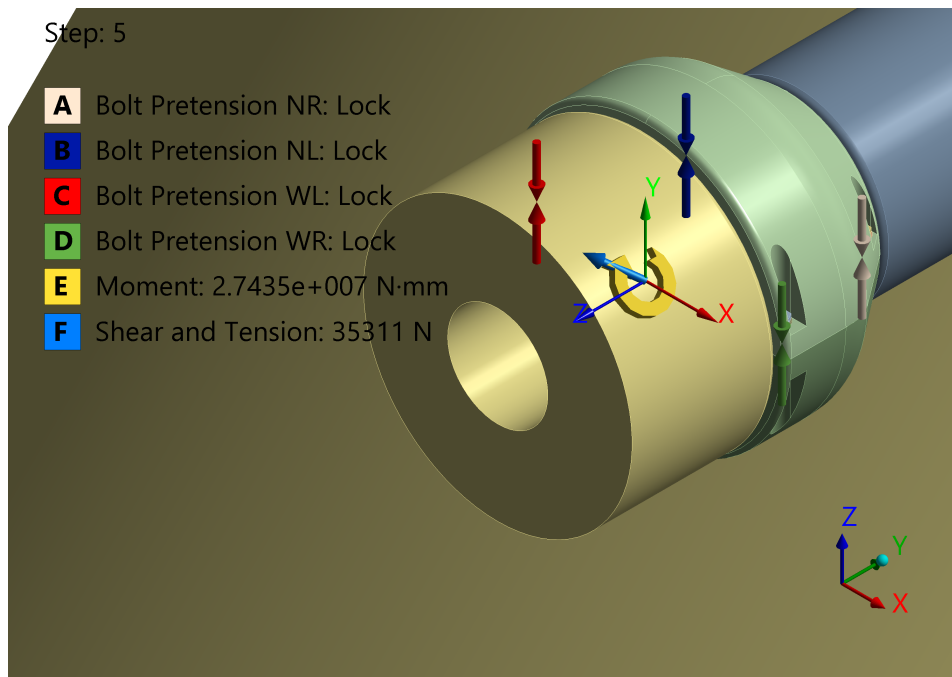
Figure 5.9: Assigned Loads CPS

5.4. Assessing Bolt Results

After applying the loadings, detailed in Table 5.3, the bolts within the knuckle were analyzed based on the shear and tensile stress. The knuckle is secured by four bolts, and the stress results were close to each other across all bolts. However, the highest stresses were observed in the bolt shown in Figure 5.12 to Figure 5.19.

5.4.1. Shear Stress

The shear stress on the bolts is obtained by looking at the shear stress in the (XZ plane). In Figure 5.12, the initial shear stress for the bolts is shown, indicating a maximum peak stress of 56.7992 MPa. Following the application of the extreme loads, as provided in Table 5.3, the shear stress reaches a maximum stress of 96.6 MPa, as illustrated in Figure 5.13.
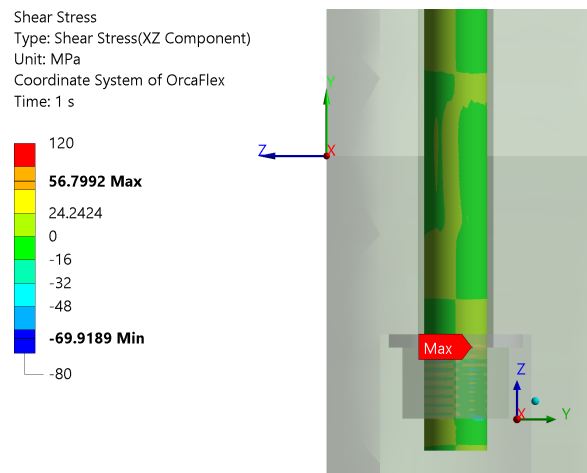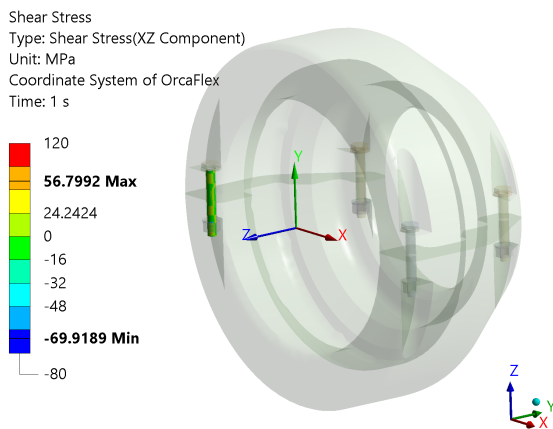
Figure 5.10: Shear Stress Bolt knuckle (only preloaded)   **Figure 5.11:** Shear Stress Bolt Zoomed (only preloaded)
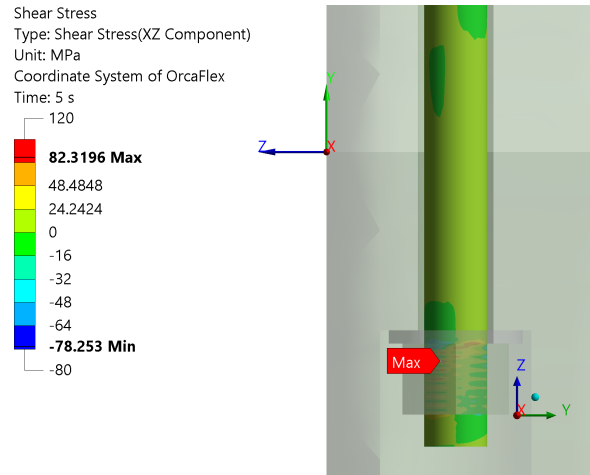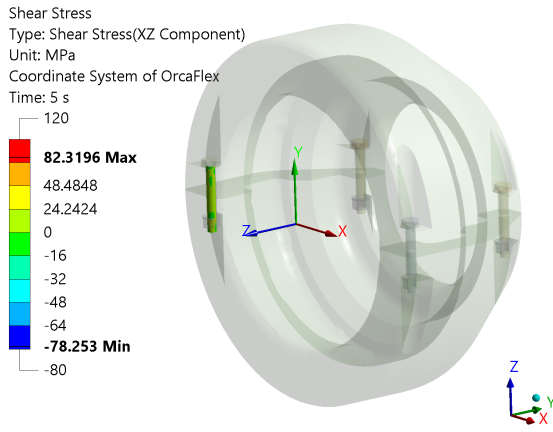
Figure 5.12: Shear Stress Bolt knuckle (after full load)   **Figure 5.13:** Shear Stress Bolt Zoomed (after full load)

Despite the applied severe loading, the stress variation remains minimal. Additionally, according to the guidelines in DNV [13], the potential shear failure is often assessed by obtaining stresses from the shear plane, which, in this case, is located between the two knuckle parts. While this location is considered to be the logical spot for shear failure.

By closer examination of the bolt, it becomes clear that the shear stress at this shear plane is practically zero. It appears that the bolted connection resists slipping. This implies that enough clamping load, which results from the preload, is applied. Since slipping is resisted even after the extreme load, shear will not be assessed as a potential failure mode, and no fatigue calculations will be included in the research.

5.4.2. Tensile Stress

The tensile stress of the bolts is obtained by looking at the normal stress in the orientation of the bolt (Z-axis). As shown in Figure 5.16, the initial stress result after applying the preload already results in a normal stress of 821.76 MPa. After applying the loads of Table 5.3, the peak stress even increases to 1221.4 MPa, as shown in Figure 5.17. Based on this significant stress variation, the bolt fatigue calculation will based on the tensile stress.
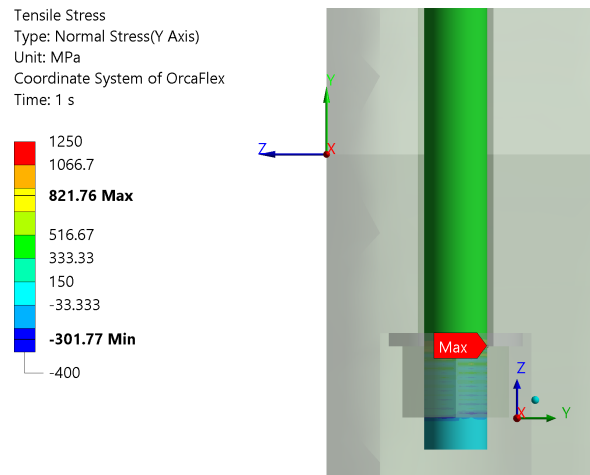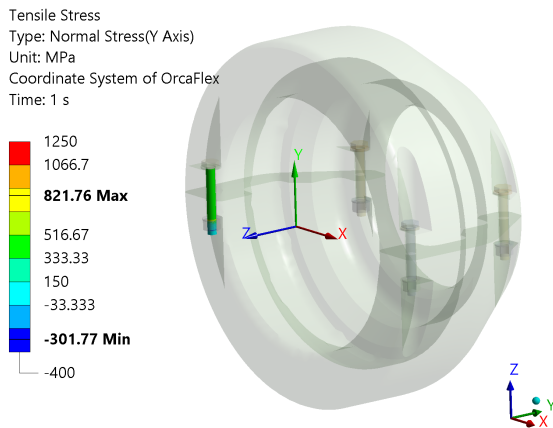
Figure 5.14: Tensile Stress Bolt Knuckle (only preloaded) **Figure 5.15:** Tensile Stress Bolt Zoomed (only preloaded)

Tensile Stress
Type: Normal Stress(Y Axis)
Unit: MPa
Coordinate System of OrcaFlex
Time: 5 s

1250
1221.4 Max
883.33
700
516.67
333.33
150
-33.333
-361.18 Min
-400

Tensile Stress
Type: Normal Stress(Y Axis)
Unit: MPa
Coordinate System of OrcaFlex
Time: 5 s

1250
1221.4 Max
883.33
700
516.67
333.33
150
-33.333
-361.18 Min
-400
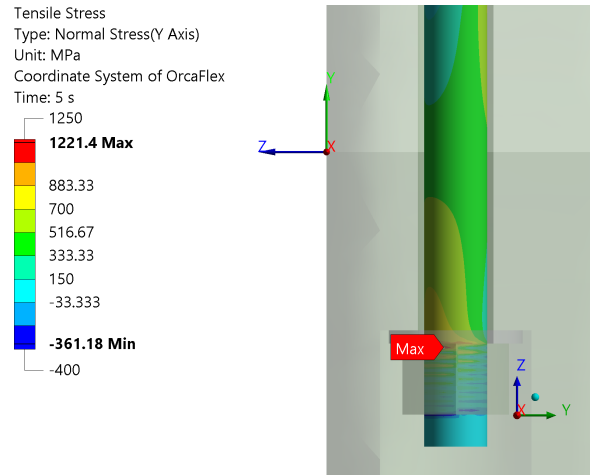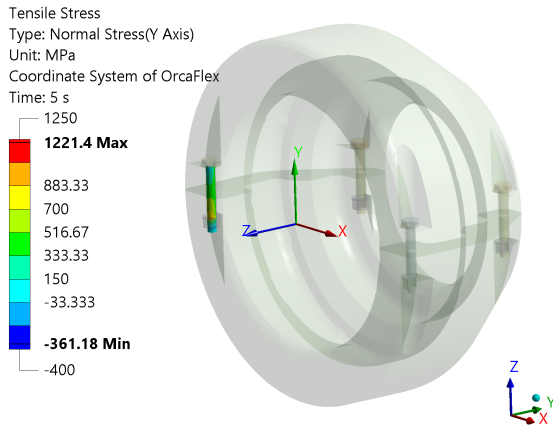
Figure 5.16: Tensile Stress Bolt Knuckle (after full load)   **Figure 5.17:** Tensile Stress Bolt Zoomed (after full load)

5.5. Peak Stress

After preloading the bolt, the crucial stress spots of the bolts become visible. Within the figures, the bolt is preloaded to its proof load of 90.43 kN, and no external forces are applied to the model. The locations where these peak stresses occur provide insight into the vulnerable areas of the bolt. High stresses are found directly under the bolt head Figure 5.18. Due to the applied geometry correction on the shaft, the threads are visible. As illustrated in Figure 5.19, it is clearly visible that the first thread encounters most of the stress. The modelled bolt in the model lacks the geometry of the threaded run-out area. Therefore, it is only logical that no higher stresses are found at that location.

The high peak stresses align with the main locations of fatigue failure, according to Lochan [63]. Which states that the main locations for fatigue cracks are distributed as follows:

- 65% the root of the first loaded thread
- 20% the thread run-out region
- 15% the head to shank radius

Type: Normal Stress(Z Axis)
Unit: MPa
Global Coordinate System
Time: 1 s
7/24/2024 3:55 PM

1554.7 Max
1323.2
1091.7
860.14
628.6
397.07
165.53
-66.002
-297.54
-529.07 Min

Type: Normal Stress(Z Axis)
Unit: MPa
Global Coordinate System
Time: 1 s
7/24/2024 3:56 PM

1181.8 Max
1007
832.17
657.37
482.57
307.77
132.97
-41.831
-216.63
-391.43 Min
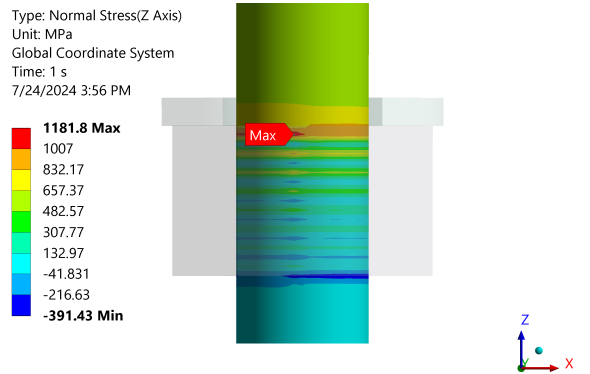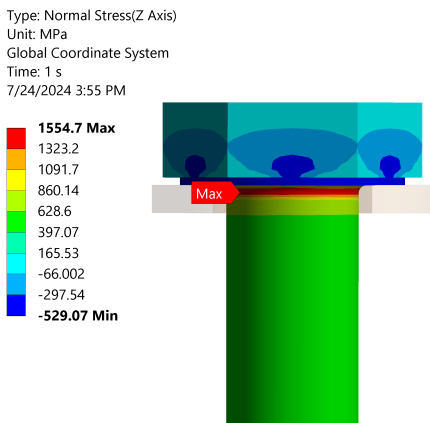
Figure 5.18: Peak stress under head of bolt (proof loaded)**Figure 5.19:** Peak stress first thread of bolt (proof loaded)

In Lehnhoff [64], a similar M16 8.8 graded bolt was loaded using linear-elastic properties to the proof load of 94.0 kN, however this model did not include a washer. This resulted in the following Stress Concentration Factor (SCF):

- Head fillet: 3.58
- Thread: 0.83 - 5.171

When applying the same proof load in the developed model, a mean stress close to 600 MPa is obtained in the middle of the bolt's shank, as expected. The peak stress under the bolt head, is shown in Figure 5.18, and has a value of 1554.7 MPa. This results in a SCF of 2.59. In Figure 5.19, the peak stress at the first thread is shown. This peak stress has a value of 1181.8 MPa, resulting in a SCF of 1.97. The thread SCF falls within the range of the thread. Regarding the head fillet, the difference in SCF could be explained to the washer, which helps to distribute the forces better.

To conclude, the peaks observed in the developed structural model are indeed significant. However, they are not unreasonably high when compared to the findings of Lehnhoff [64]. The comparison suggests that while the peak stress values are substantial, they fall within a plausible range.

6

Fatigue Limit States Analysis

The assessment of bolt damage for each sea state is obtained within the hydrodynamic model. To assess the damage, the hydrodynamic model requires the stresses of the bolt in a time domain to evaluate the stress ranges. An external function is incorporated into the model to obtain the bolt stress. This chapter details how the correlation formula was obtained and integrated. It continues by explaining how the hydrodynamic model calculates the damage based on the selected S-N curve. It concludes with the evaluation of the bolt's fatigue life, correlating to the exposure time.

6.1. Fatigue Assessment
Although there are several methods to assess the fatigue life of bolts [63]. The nominal stress approach is the most widely used fatigue assessment method to estimate the endurance of bolts [65]. The approach simplifies the complex stress distribution, to a single average stress value, making the fatigue analysis more manageable.

While the method is widely used in the offshore industry, the fatigue classes and categories provided in the code are based on constant amplitude testing [66]. However, in a hydrodynamic environment, the component is often subjected to variable amplitude loading. Additionally, omitting certain details, like the geometry's specifics, can lead to variability in the fatigue assessment results. Even the difference between fine and normal threads can have an effect [65]. Nevertheless, the approach offers a balance between simplicity and safety and is therefore considered a practical choice.

6.2. Regression Model
To find the correlation between the loadings at the CPS and the tensile loading at the bolt, over 1000 cases were implemented within the structural model, as explained in subsection 5.2.3.

By combining the orthogonal shear components, x-shear and y-shear, the resultant shear was calculated using Equation 6.1. Similarly, using the orthogonal bending moment components, x-moment and y-moment, the resultant moment was calculated using Equation 6.2. This way, the orthogonal component variables are still included but combined, which reduces the total number of variables in the regression model, resulting in a more simplified regression model.

$$\tau = \sqrt{\tau_x^2 + \tau_y^2} \tag{6.1}$$

$$M = \sqrt{M_x^2 + M_y^2} \tag{6.2}$$

6.2.1. Testing and Validating the regression model
The various regression models were validated using standard functions within Python, as detailed in Appendix E.1. Each model splits the data into two data sets: the training set and the test set. Following

the guidelines of Géron [67], 80% of the obtained data was used for training, and 20% was reserved for testing. This allows for an effective validation of the regression models.

Several methods are available that provide insights into different aspects of the model. For the developed linear regression models, the Mean Squared Error (MSE), R^2 and the adjusted-R^2 were assessed.

The MSE value represents how close a fitted line is to the data points. A lower MSE suggests a better fit to the data. The R-squared, also referred to as the coefficient of determination, quantifies the proportion of variance for the dependent variable that is predictable from the independent variables within the regression model. In other words, it shows how much of the result can be explained by the input variables. However, R-squared is most suitable for simple linear regression. Since the model uses multiple input variables, it is considered a multiple linear regression model. For multiple linear regression models, the R-squared increases even though an independent variable is insignificant. The adjusted R-squared is therefore utilized, which only increases when an independent variable is significant [68].

$$MSE = \frac{\sum \left(y_i - \hat{y}_i\right)^2}{n} \tag{6.3}$$

$$R^2 = 1 - \frac{\sum \left(y_i - \hat{y}_i\right)^2}{\sum \left(y_i - \bar{y}\right)^2} \tag{6.4}$$

$$R^2{}_{\text{Adjusted}} = 1 - \frac{\left(1 - R^2\right)\left(n - 1\right)}{n - p - 1} \tag{6.5}$$

where: $\bar{y}$ = is the mean of the y values
y_i = is the i$^{\text{th}}$ observed value
$\hat{y}_i$ = is the corresponding predicted value
n = the number of observations
p = number of variables

The linear regression models were tested on the MSE, the R-squared and R-squared (adjusted). An overview of the four different regression models, including differences in polynomial degree and input variables, is illustrated in Table 6.1. Models 1 and 2 use the moments and shear as individual orthogonal components, while models 3 and 4 utilize the combined orthogonal components.

	Utilized Variable:								Validation Result:		
Model	xshear	yshear	ztension	xmoment	ymoment	resultant shear	resultant moment	polynominal degree	MSE	R^2	R^{2}Adjusted
1	x	x	x	x	x			1	2.27	0.48	0.47
2	x	x	x	x	x			2	0.71	-	-
3			x			x	x	1	2.13	0.52	0.51
4			x			x	x	2	0.62	-	-

Table 6.1: Validating Regression models

6.2.2. Correlation Formula
After validating the different regression models, model 4, which utilizes the resultant shear and moment with a polynomial degree of 2, was found to be the suitable option. It showed that using resultant shear and resultant moment variables increased the R-squared. Furthermore, it provided the lowest MSE. The regression model provided us with the following correlation formula:

$$
\begin{aligned}
F_{t,bolt}(t) = {}& 101.4656 + (6.2988)T(t) + (0.3074)\tau(t) - (5.4864)M(t) + (0.5868)T(t)^2 - (0.3734)T(t) \cdot \tau(t) \\
& - (0.4080)T(t) \cdot M(t) + (0.0862)\tau(t)^2 - (0.1051)\tau(t) \cdot M(t) + (0.2695)M(t)^2
\end{aligned}
\tag{6.6}
$$

where: $F_{t,bolt}$ = Tensile Force Bolt(kN)
$\quad\quad\quad T$ = Effective Tension (kN)
$\quad\quad\quad \tau$ = Combined Shear Force (kN)
$\quad\quad\quad M$ = Combined Bending Moment (kNm)

6.3. External OrcaFlex Function

After the correlation formula was found, an external Python function was developed. This function, detailed in section E.2, takes the required loading results and uses it to calculate the tensile force in the bolt. To calculate the tensile stress at the bolt Equation 6.7 was utilised and included in the Python code.

$$\sigma_{bolt}(t) = \frac{F_{t,bolt}(t)}{A_t} \tag{6.7}$$

where: $\quad \sigma_{bolt}$ = Stress Bolt (kPa)
$\quad\quad\quad F_{t,bolt}$ = Tensile Force Bolt(kN)
$\quad\quad\quad A_t$ = Tensile Stress Area (m^2)

In Figure 6.1a, an example of such a bolt stress time history is shown. The correlation between the bolt stress and the loadings is visible when examining the relatively large fluctuations of the bolt stress graph. For example, a notable tension peak in all the external load functions, illustrated with the red arrow in Figure 6.1b, Figure 6.1c, and Figure 6.1d at 4596.8 seconds, corresponds with a noticeable peak of the nominal bolt stress at the same time shown in Figure 6.1a. Using the same external function, the nominal bolt stress in a time domain for all sea states and directions for the entire 3-hour duration was obtained.

(a) Bolt Stress

(b) Tension

(c) Shear

(d) Bend Moment
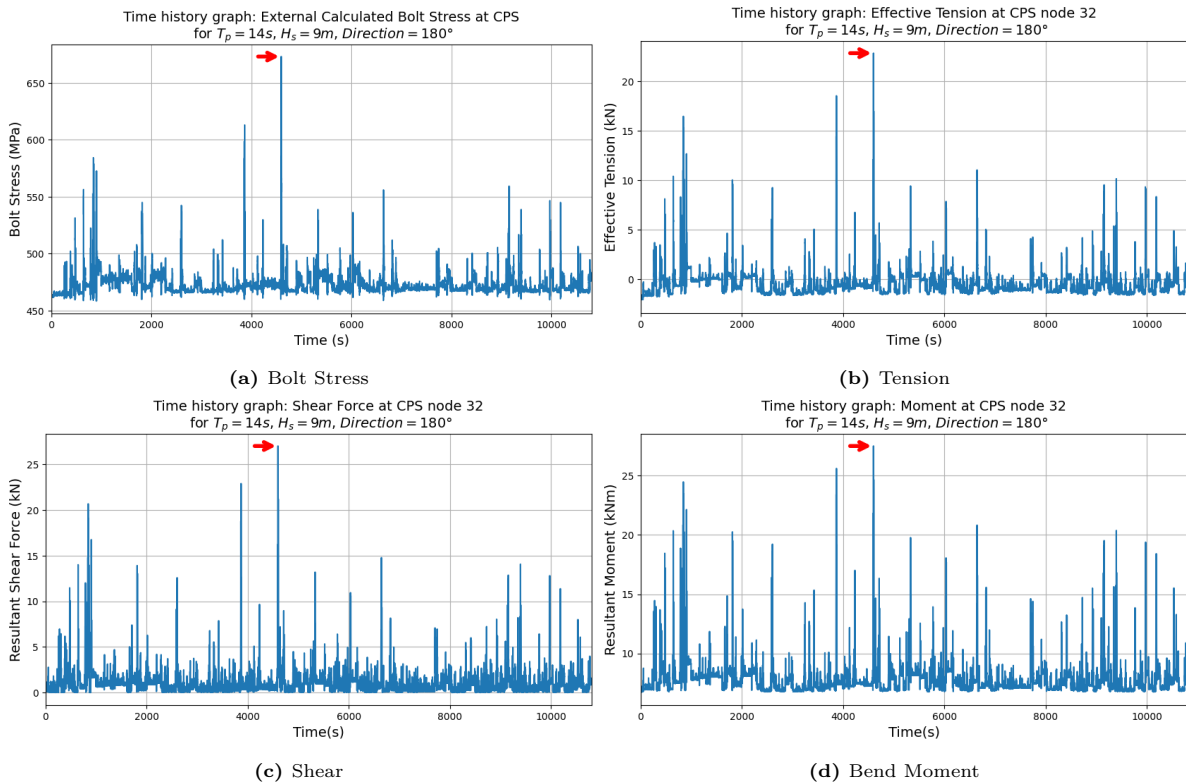
Figure 6.1: Bolt Stress and correlated variables

6.4. Damage calculation

Now that the bolt stresses are estimated for each sea-state, as Figure 6.1a shows. The damage can be calculated.

6.4.1. Rainflow Counting

To perform a fatigue analysis on irregular loading, the model uses a rainflow counting method. This technique is used to extract the number of cycles and find the range of the bolt stress. The process begins with applying the rainflow counting method to the nominal stress time domain data. The stress cycles are identified and counted based on based on their ranges. Next, these cycles are organized into a rainflow counting plot, where each stress range is binned according to its range. This helps to analyze how frequently each stress range occurs. This method is widely used and well documented in the literature, including in Amzallag [69].

6.4.2. S-N curve

As previously discussed, the fatigue calculation is based on an S-N curve. The S-N curve is chosen from the DNV [13], focusing on fatigue at offshore structures. The S-N curve is based on the nominal stress approach. Since shear stress is less significant compared to tensile stress, the fatigue calculation is only based on the tension within the bolt.

As Figure 6.2 shows, there are two available S-N curves (F1 and G) for tensile at bolts. Given that the bolts within the CPS knuckle are galvanised, to provide additional corrosion protection, S-N curve G was taken. For reference, Figure 6.3 shows the different S-N curves. The S-N curve G is highlighted in blue. The corresponding values used for the S-N curve in the hydrodynamic model are given in Table 6.2.

Figure 6.2: S-N Curve Detail [13]

S-N curve	N < 10^6 cycles		N ≤ 10 ^{6}cycles		Fatigue limit at 10^7 cycles (MPa)	Stress Concentration Factor
	m_1	$\log(a_1)$	m_2	$\log(a_2)$		
G	3.0	10.998	5	14.330	29.24	1.80

Table 6.2: S-N Curve Properties

Stress Concentration Factor

As suggested in Table 6.2, a SCF of 1.8 is utilized. This accounts for the hydrogen cracks that are caused by the zinc coding, as well as the possibility of an uneven coating thickness, which can increase the stress concentration.
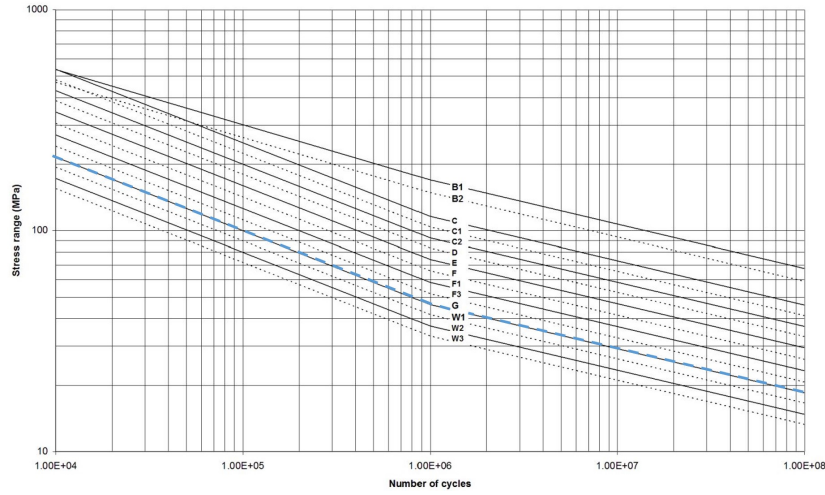
Figure 6.3: S-N curves in seawater with cathodic protection [13]

6.4.3. Palmgren-Miner Rule

After the Rainflow counting is performed and the S-N curve has been assigned, the amount of damage can be calculated. The Palmgren-Miner rule is utilised for damage calculations. This rule predicts fatigue failure by a summation of the stress amplitudes. This rule assumes to be linear cumulative [70].

$$D = \sum_{i=1}^{k} \frac{n_i}{N_i} \tag{6.8}$$

Here, D represents the accumulated damage, n_i represents the number of cycles that are applied at the ith stress level σ_i, N_i is the fatigue life at σ_i, and k is the number of blocks into which the recorded stress has been placed.

6.5. Lifetime calculation

To assess the expected lifetime of the bolt, all different sea directions are evaluated. Since the process is consistent across all directions, the process of the 90-degree wave is detailed as an example.

6.5.1. Damage Tables

The calculated damages for each simulation case can be assigned to the wave scatter diagram, which results in Table 6.3. This table shows that for many sea-states, no damage to the bolt was inflicted. It is only for the higher sea states that damage at the bolt was observed. To reduce the amount of simulations not all sea-states were simulated, and therefore their damage could not be estimated, the excluded damage is represented in the graph with a -. Since damage was observed only for the extreme sea states, it can be assumed reasonably to exclude the lower sea states, since no damage is expected.

6.5.2. Exposed Time

Based on the wave scatter diagram, Table 4.4, the probability for each sea state can be calculated, using Equation 6.9

$$\text{Probability of occurrence} = \frac{\text{Number of occurrences}}{\text{Total number of occurrences}} \tag{6.9}$$

Since the directions are simulated per 30 degrees, 12 different directions can be distinguished. Since the orientation of the CPS in this case study is not defined, it has been assumed that all directions have an equal chance of occurring. Given this, the total exposure time can be calculated using Equation 6.10.

$$\text{Exposed time} = \frac{\text{Probability of occurrence} \cdot \text{ simulation time}}{12} \tag{6.10}$$

HS/Tp	<2	2	4	6	8	10	12	14	SUM
9	-	-	0	0	0	2.025E-06	1.467E-05	3.038E-05	4.708E-05
8	-	-	0	0	0	2.737E-07	4.680E-06	7.612E-06	1.2567E-05
7	-	-	0	0	0	0	2.021E-06	1.814E-06	2.016E-06
6	-	-	0	0	0	0	0	3.593E-07	3.593E-07
5	-	-	0	0	0	0	0	0	0
4	-	-	0	0	0	0	0	0	0
3	-	-	0	0	0	0	0	0	0
2	-	-	0	0	0	0	0	0	0
1	-	-	0	0	0	0	0	0	0
< 1	-	-	-	-	-	-	-	-	-
SUM	-	-	0	0	0	2.299E-06	1.955E-05	4.017E-05	6.202E-05

Table 6.3: Damage (90 degrees)

HS/Tp	<2	2	4	6	8	10	12	14	SUM
9	0	0	0	0	0	0	0.000001	0.000006	0.000007
8	0	0	0	0	0	0.000005	0.000077	0.000009	0.000090
7	0	0	0	0	0	0.000162	0.000203	0.000023	0.000387
6	0	0	0	0	0.000031	0.000847	0.000238	0.000030	0.001147
5	0	0	0	0	0.000607	0.002691	0.000075	0.000017	0.003389
4	0	0	0	0.000024	0.006375	0.003696	0.000037	0.000020	0.010151
3	0	0	0	0.003373	0.019256	0.001810	0.000064	0.000025	0.024527
2	0	0	0.001036	0.033911	0.023369	0.002209	0.000188	0.000006	0.060718
1	0	0.000324	0.046744	0.058403	0.020262	0.001401	0.000030	0	0.127165
< 1	0.000003	0.002547	0.015952	0.003628	0.000257	0.000031	0.000001	0	0.022419
SUM	0.000003	0.002871	0.063731	0.099339	0.070156	0.012852	0.000914	0.000135	0.25

Table 6.4: Exposed hours (90 degrees)

6.5.3. Total Damage

With the total damage and time of exposure now known for all sea states, the total damage that occurs in 3 hours can now be calculated. This is done by multiplying the damage, see Table 6.3, with the exposed time of the corresponding direction, see Table 6.4. This results in Table 6.5. As Table 6.5 shows, the total damage for the bolt in the 90-degree direction is 7.1444E-10. Similarly, the total damage for the other directions has been calculated. The results for all directions are presented in Appendix D.

When combining all the total damage results and assuming similarity between directions, as discussed in subsection 4.3.1, the total damage can be obtained for all different directions. (see Table 6.6).

With the total damage now known for 3 hours, the total lifetime of the be bolt can then be calculated using Equation 6.11.

$$\text{Lifetime (hours)} = \frac{1}{\text{Total Damage}} * \text{Time Simulation (3 hours)} \tag{6.11}$$

This results in a lifetime of 57,208,237 hours, which is equal to a total lifetime of 6526 years. This estimated fatigue life far exceeds the typical design life of an offshore wind turbine, which is normally between 25 to 35 years. Even when applying a DFF of 10, as recommended by [61], resulting in an allowable fatigue life of 350 years, the expected life still surpasses it. Based on these findings, it seems that the selected bolt cannot only withstand the loads but also offer a considerable margin of safety.

HS/Tp	<2	2	4	6	8	10	12	14	SUM
9	-	-	0	0	0	0	1.442E-11	1.792E-10	1.937E-10
8	-	-	0	0	0	1.346E-12	3.590E-10	6.737E-11	4.277E-10
7	-	-	0	0	0	0	4.094E-11	4.104E-11	8.199E-11
6	-	-	0	0	0	0	0	1.095E-11	1.099E-11
5	-	-	0	0	0	0	0	0	0
4	-	-	0	0	0	0	0	0	0
3	-	-	0	0	0	0	0	0	0
2	-	-	0	0	0	0	0	0	0
1	-	-	0	0	0	0	0	0	0
< 1	-	-	-	-	-	-	-	-	
SUM			0	0	0	1.346E-12	4.144E-10	2.986E-10	7.1444E-10

Table 6.5: Total damage (90 degrees)

Direction (deg)	Total Damage (-)
0	$1.471 \cdot 10^{-8}$
30	$9.779 \cdot 10^{-9}$
60	$2.582 \cdot 10^{-11}$
90	$7.144 \cdot 10^{-10}$
120	$6.384 \cdot 10^{-11}$
150	$1.228 \cdot 10^{-9}$
180	$1.471 \cdot 10^{-8}$
210	$9.779 \cdot 10^{-9}$
240	$2.582 \cdot 10^{-11}$
270	$1.102 \cdot 10^{-10}$
300	$6.384 \cdot 10^{-11}$
330	$1.228 \cdot 10^{-9}$
Sum:	$5.244 \cdot 10^{-8}$

Table 6.6: Total damage per direction for 3 hours

6.6. Analyzing the expected Fatigue lifetime

While the estimated fatigue lifetime might appear to be extreme, it can be considered reasonable given the methodology used. Since only for severe sea-states minor damage was observed, and these severe sea-states do not occur frequently.

The lack of available data on bolt lifetime within a CPS or similar subsea object makes it difficult to compare the estimated lifetime results. However, there is one report that assessed the fatigue lifetime of bolts within a CPS. This report also utilizes DNV [13] to obtain the S-N curve. It estimated that the bolt would remain undamaged throughout its entire lifetime, thereby suggesting an unlimited lifetime expectancy. Although this assessment is based on a somewhat different CPS design, it is improbable that the bolt would endure indefinitely in seawater. Alternative failure modes, aside from tensile stress, must be considered. While an estimated lifetime of 6,526 years is significant, further research is necessary to validate this estimation and address potential limitations before drawing definitive conclusions.

7

Conclusions and Recommendations

This chapter begins by outlining the main observations of the research. In the following subsections, answers to main research question and sub questions (see section 1.3) are summarized respectively.

7.1. Conclusions

On the basis of the literature research, it can be concluded that the failure of the CPS data is not publicly accessible. Limited reports emphasised on relatively large amount of failures seen at subsea cables within the offshore industry. Mostly news articles, reports, and experienced personal from the offshore industry confirm that failures of the CPS are quite common, leading to costly maintenance need. Because of lack of scientific studies, the root cause of CPS failure is still unclear. Hence, this research serves as an initial attempt to assess the integrity of such CPSs. Within this research, one of the most important research needs was identified as the critical limit states associated with the bolted connection within the system. Considering this aspect the following main research question was identified:

What are the critical limit states associated with the bolted connections within the cable protection system in subsea environments?

In order to answer the above research questions effectively four sub-questions were set (see section 1.3). This subsection provides answers to the sub questions.

1. *What are the critical locations within a cable protection system where the bolted connections are most susceptible to failure?*

   To assess the critical limit states of the bolted connection within the CPS, the first step was to identified the critical locations within the CPS. Next step was to develop a hydrodynamic model to simulate the CPS in a subsea environment which estimated the expected loads on the critical section of the CPS. In this stage the loading was calculated on the basis of sea waves and currents. The results, showed that the maximum shear and moments were observed nearby the entry hole, which is aligned with the findings of passed literature.

   The results also showed that the critical section i.e. entry hole experiences the largest fluctuation in terms of calculated forces and moments, making it potentially more susceptible to fatigue failure. The maximum range of loading fluctuation at the critical location was observed for the maximum sea state loading condition which is directed perpendicular to the CPS. Within the bolted connection the model showed that the critical location is the latching knuckle, located near the entry hole. In addition, the model showed that the excessive motion of the CPS across the scour protection causes high loading values. This observation suggest that researches should propose strategies, to mitigate loadings at the identified critical location in order to improve the stability of the CPS, which will result in improved lifetime.

2. *How do various loading and movement conditions affect the bolted connections within the system?*

   A structural model was developed to perform a detailed structural analysis of the bolts within the

latching knuckle of the CPS. The developed model proved to be an important tool in this research, as a deeper insight into the effect of the loadings on the bolted connection within the system was able to be obtained. The analysis revealed that even when extreme loading was applied, no substantial shear stress in the shear plane occurred due to sufficient clamping. However, a significant impact on the tensile stress of the bolt was observed. In order to simulate real in-situ behaviour of the CPS instead of applying the various loadings separately, they were applied simultaneously. Therefore, this research has not been able to identify the most critical loading conditions.

3. *What fatigue limit states could potentially compromise the integrity of these bolted connections?*

Based on the results from the structural model it could be concluded, that various loads significantly impact the bolt's tensile stresses as compared to shear stresses. With the obtained values of stresses, nominal stress was used to calculate the expected fatigue life of the bolts. On the basis obtained data, it can be concluded that the tensile fatigue values are far more critical as compared to shear fatigue values.

4. *Based on the proposed methodology, what can be said about the expected lifetime of the bolts?*

Based on the results from the hydrodynamic model, critical combination of loads were identified as input parameters for the structural model. A parametric analysis considering the obtained loading combination was done to obtain a database of CPS loadings. After the database was created, a statistical (regression) analysis was done between the CPS loading results and the bolt tensile force. A total of four regression models were developed in this research with different combinations of polynomial degree and different combinations of loading as input variables. The developed regression equations were further used in the hydrodynamic model to obtain the bolt stress history in time domain. The obtained history was then used to estimate fatigue damage of the bolt for different types of sea state. The final estimate of expected fatigue life was obtained by summing the total damage caused by different types of sea state.

The results obtained from the analysis showed that no significant damage occurred for the sea states that were considered in this research. Hence, it can be concluded that the lifetime of bolts will sustain for the entire design period provided all other factors such as chemical processes, loosening of the bolt, unfavorable environmental surrounding conditions, inproper installment etc. are neglected.

In summary, this research provides a framework for assessing fatigue failure for components subjected to irregular external loadings on the basis of hydrodynamic and structural models analyzed in a staggered approach. It is noted that proposed approach is not only limited to the bolts and CPS designs. Other applications of the proposed approach are possible.

7.2. Recommendations

The presented approach provides a foundation for fatigue calculations within a subsea environment. This section aims to provide recommendations for future research that was not possible in the current research.

7.2.1. Hydrodynamic Analysis

In this research the VIV are not integrated within the model. It can be expected that flow around the CPS induces vortices, which could result in additional damage. To account for these vortices in hydrodynamic model, different VIV models can be applied. It is highlighted that the calculation of fatigue analysis in commercially available dynamic analysis packages could be challenging, because they provide data in frequency domain rather time domain.

In this research the developed model considers both the seabed and scour protection as flat surfaces. In reality, the seabed is rough, which restricts the motion of the CPS. Hence, in the future research a more realistic seabed surface could be considered.

In this research, to carry out simulations within a reasonable timeframe, only a limited number of simulation were carried. A consistent current velocity was applied, with the same direction as the wave.

This assumption does not hold up in reality. By using more specific data, the predictions could be improved in future research.

7.2.2. Structural Analysis

In this research bolts with only one material was considered. For future research, bolt with higher strength classes which could be favourable initially, however a increased risk of HISC should be studied. Similarly, bolts with galvanized materials should be carefully investigated as they protect against corrosion but seem to have less fatigue life.

In this research only linear-elastic materials were considered. This can result in inaccurate estimation of peak stresses. To obtain stress values that are closer to reality, future research can include non-linear material properties. Furthermore, a real thread geometry should be considered for better prediction of peak stresses.

A parametric study into the effect of a variation in the preload would be valuable. Since the correct torque application on a bolt does not always produce the expected pretension value, variable preloads may introduce additional fluctuating stresses into the bolt that could affect the fatigue life of the joint. Hence, these aspects could be studied in future research.

7.2.3. Fatigue Limit State Analysis

In this research, the Nominal Stress Approach, was utilized. However, there are more available option to conduct a fatigue analysis. Improved peak stress results, by incorporating a non-linear stress-strain curve for example allows for the employment of such fatigue assessment methods, that could potentially offer new insights regarding the bolt's failure.

The Structural Stress Approach is such an alternative fatigue approach that offers a more detailed view of stress distribution across the structure, improving the understanding of stress behavior within the system. Another method is the Notch Stress Approach. Although it is not a standardized fatigue method, it has the advantage of utilizing high peak stresses for fatigue assessment. Which makes it particularly useful for analyzing locations with high-stress concentrations.

Moreover, the S-N curve utilized in this research is based on the nominal stress of galvanized bolts, which may not fully capture the specific characteristics of the bolts. To further refine fatigue assessments, future research should consider developing S-N curves tailored specifically to the bolt type used. While the S-N curves provided by DNV and Eurocodes offer valuable guidance, they may not account for all the nuances of specific bolt types. Conducting additional experiments with bolts in seawater could lead to more precise and reliable data for fatigue assessments.

7.2.4. Leveraging Failures

Future research should encouraging greater transparency within the industry, to find the root causes of CPS failures. Researchers should aim to gather detailed data on the locations of failed CPS components and, where possible, retrieve the damaged or broken components for thorough examination. Such efforts could lead to the development of additional mitigation measures for currently installed CPS. After all, failures should not be hidden but rather embraced as valuable lessons to allow for improvement and innovation.

References

[1] Katherine Calvin et al. *IPCC, 2023 Climate Change 2023: Synthesis Report*. Tech. rep. Intergovernmental Panel on Climate Change, July 2023. DOI: 10.59327/IPCC/AR6-9789291691647. URL: https://www.ipcc.ch/report/ar6/syr/.

[2] International Renewable Energy Agency. *Renewable Power Generation*. Tech. rep. 2023. URL: www.irena.org%20https://mc-cd8320d4-36a1-40ac-83cc-3389-cdn-endpoint.azureedge.net/-/media/Files/IRENA/Agency/Publication/2023/Aug/IRENA_Renewable_power_generation_costs_in_2022.pdf?rev=3b8966ac0f0544e89d7110d90c9656a0 (visited on 07/31/2024).

[3] Allianz Commercial. *A turning point for offshore wind Global opportunities and risk trends*. Tech. rep. 2023. URL: https://www.allianz.com/content/dam/onemarketing/azcom/Allianz_com/press/document/Allianz-Commercial_A-turning-point-for-offshore-wind.pdf (visited on 07/31/2024).

[4] Riccardo Felici and Daniele Caruso. *Cable Protection Systems and Submarine Cable Failures*. Tech. rep. 2022. URL: https://abl-group.com/all-media/news/abl-group-releases-downloadable-whitepaper-on-cable-protection-systems-failures/ (visited on 07/31/2024).

[5] David Craik. *Growing findings of offshore cable damage hike pressure on protection*. 2021. URL: https://www.reutersevents.com/renewables/wind/growing-findings-offshore-cable-damage-hike-pressure-protection (visited on 07/31/2024).

[6] Offshore Independents. *Interviews with subsea cable experts*. 2023.

[7] Rafael Loureiro Tanaka et al. "Bending Stiffener Design Through Structural Optimization". In: *Volume 3: Pipeline and Riser Technology*. ASMEDC, Jan. 2009, pp. 411–418. ISBN: 978-0-7918-4343-7. DOI: 10.1115/OMAE2009-79505.

[8] [Confidential]. *CPS Technical Report*. Tech. rep. 2022.

[9] Richard Budynas and J. Keith Nisbett. *Shigley's Mechanical Engineering Design*. 10th edition. 2015. ISBN: 978-0-07-339820-4.

[10] Shun Peng Zhu et al. "Mean stress effect correction in strain energy-based fatigue life prediction of metals". In: *International Journal of Damage Mechanics* 26.8 (Nov. 2017), pp. 1219–1241. ISSN: 15307921. DOI: 10.1177/1056789516651920.

[11] Ivan Okorn et al. "Analysis of Additional Load and Fatigue Life of Preloaded Bolts in a Flange Joint Considering a Bolt Bending Load". In: *Metals* 11.3 (Mar. 2021), p. 449. ISSN: 2075-4701. DOI: 10.3390/met11030449.

[12] EN 1993-1-9. *Eurocode 3: Design of steel structures - Part 1-9: Fatigue*. Tech. rep. 2005.

[13] DNV-RP-C203. *Fatigue design of offshore steel structures*. DNV, 2019.

[14] Thomas Worzyk. "Submarine Power Cables: Design, Installation, Repair, Environmental Aspects". In: *Power Systems* 39 (2009). ISSN: 16121287. DOI: 10.1007/978-3-642-01270-9.

[15] Narakorn Srinil. "Cabling to connect offshore wind turbines to onshore facilities". In: *Offshore Wind Farms*. Elsevier, 2016, pp. 419–440. DOI: 10.1016/B978-0-08-100779-2.00013-1.

[16] E Gulski et al. "Discussion of electrical and thermal aspects of offshore wind farms' power cables reliability ". In: (2021). DOI: 10.1016/j.rser.2021.111580. URL: https://doi.org/10.1016/j.rser.2021.111580.

[17] JIP Haspro. *Handbook of Scour and Cable Protection Methods*. Tech. rep. 2023. URL: https://publications.deltares.nl/Deltares250.pdf (visited on 07/31/2024).

[18] Ahmed Reda et al. "Design of subsea cables/umbilicals for in-service abrasion - Part 2: Mechanisms". In: *Ocean Engineering* 234 (Aug. 2021), p. 109098. ISSN: 0029-8018. DOI: 10.1016/J.OCEANENG.2021.109098.

[19] Adnan Durakovic. *Ørsted and Tekmar Tackle Array Cable Issue at Race Bank Offshore Wind Farm | Offshore Wind*. 2021. URL: `https://www.offshorewind.biz/2021/05/04/orsted-and-tekmar-tackle-array-cable-issue-at-race-bank-offshore-wind-farm/` (visited on 07/31/2024).

[20] Ahmed Reda et al. "Design and installation of subsea cable, pipeline and umbilical crossing interfaces". In: *Engineering Failure Analysis* 81 (Nov. 2017), pp. 193–203. ISSN: 13506307. DOI: `10.1016/j.engfailanal.2017.07.001`.

[21] Tramontana Engineering. *Failure of Cable Protection Systems*. 2021.

[22] Tekmar. *Tekmar Products*. URL: `https://tekmar.co.uk/product/` (visited on 07/31/2024).

[23] saVRee. *Flange Nuts and Bolts Explained (Fasteners)*. URL: `https://savree.com/en/encyclopedia/flange-nuts-and-bolts` (visited on 07/31/2024).

[24] G Majzoobi, G Farrahi, and N Habibi. "Experimental evaluation of the effect of thread pitch on fatigue life of bolts". In: *International Journal of Fatigue* 27.2 (Feb. 2005), pp. 189–196. ISSN: 01421123. DOI: `10.1016/j.ijfatigue.2004.06.011`.

[25] MaxPro. *Bolted Joint Design: The Difference Between Tension, Shear and Bending Joints*. 2018. URL: `https://www.maxprocorp.com/blog/the-difference-between-tension-shear-and-bending-joints/` (visited on 07/31/2024).

[26] F. C. Campbell. "Fatigue and Fracture - Understanding the Basics". In: 2012. ISBN: 978-1-61503-976-0.

[27] Ansys. *The Mechanics of Bolted Joints*. 2020. URL: `https://courses.ansys.com/wp-content/uploads/2022/12/Mechanics_of_Bolted_Connections.pdf` (visited on 07/31/2024).

[28] Sandro Griza et al. "The effect of bolt length in the fatigue strength of M24×3 bolt studs". In: *Engineering Failure Analysis* 34 (Dec. 2013), pp. 397–406. ISSN: 13506307. DOI: `10.1016/j.engfailanal.2013.09.010`.

[29] Inge Lotsberg. "Design of Bolted and Threaded Connections". In: *Fatigue Design of Marine Structures*. Cambridge University Press, Mar. 2016, pp. 379–399. DOI: `10.1017/cbo9781316343982.015`.

[30] Y. Q. Ni, X. W. Ye, and J. M. Ko. "Monitoring-Based Fatigue Reliability Assessment of Steel Bridges: Analytical Model and Application". In: *Journal of Structural Engineering* 136.12 (Dec. 2010), pp. 1563–1573. ISSN: 0733-9445. DOI: `10.1061/(ASCE)ST.1943-541X.0000250`.

[31] Maiada S. Abdelrahman, Waleed Khalifa, and Mahmoud T. Abdu. "Failure Analysis of Fatigue Failed M20 Class 8.8 Galvanized Steel Bolt". In: *Engineering Failure Analysis* 150 (Aug. 2023), p. 107304. ISSN: 13506307. DOI: `10.1016/j.engfailanal.2023.107304`.

[32] Helen Bartsch and Markus Feldmann. "Reassessment of fatigue detail categories of bolts and rods according to EC 3-1-9". In: *Journal of Constructional Steel Research* 180 (May 2021), p. 106588. ISSN: 0143974X. DOI: `10.1016/j.jcsr.2021.106588`.

[33] Hardlock. *Why do bolts fail from fatigue?* URL: `https://hardlock-nut.com/technical-info/fatigue-failure/` (visited on 07/31/2024).

[34] Inge Lotsberg. "Fatigue Design of Marine Structures". In: Cambridge: Cambridge University Press, 2016. ISBN: 9781107121331. DOI: `10.1017/CBO9781316343982`. URL: `https://www-cambridge-org.tudelft.idm.oclc.org/core/books/fatigue-design-of-marine-structures/46B500FE3D352ABF5FE2ABF9EB73B1D7`.

[35] *Metocean Report: Gemini [SECURED]*. Tech. rep. DHI Wasy, 2012.

[36] DNV-RP-C205. *Environmental conditions and environmental loads*. DNV, 2021.

[37] DNV-RP-0360. *Subsea power cables in shallow water*. DNV, 2016.

[38] DNV-CG-0130. *Wave loads*. DNV, 2021.

[39] DNVGL-ST-0437. *Loads and site conditions for wind turbines*. DNV, 2016.

[40] DNV-RP-C101. *Structural design of offshore units*. DNV, 2023.

[41] Orcina. *OrcaFlex Manual version 11.3f.* 2023. URL: `https://www.orcina.com/webhelp/OrcaFl ex/` (visited on 07/31/2024).

[42] *OrcaFlex - dynamic analysis software for offshore marine systems.* 2023. URL: `https://www. orcina.com/orcaflex/` (visited on 07/31/2024).

[43] DNV-RP-F109. *On-bottom stability design of submarine pipelines, cables and umbilicals.* DNV, 2021.

[44] Alan Dobson. "Challenges Associated With High Voltage Dynamic Inter Array Cables". In: *International Conference on Offshore Mechanics and Arctic Engineering.* Vol. 86854. American Society of Mechanical Engineers. 2023, V003T04A024.

[45] Rijksoverheid. URL: `https://windopzee.nl/imagemaps/kaart-waar-wanneer/ten-noorden- van-de-waddeneilanden/` (visited on 07/31/2024).

[46] offshoreWIND. *Tekmar TekLink Installed on Gemini Offshore Wind.* 2015. URL: `https://ww w.offshorewind.biz/2015/08/18/tekmar-teklink-installed-on-gemini/` (visited on 07/31/2024).

[47] Ion Lizarraga-Saenz et al. "Study of the influence of met-ocean data in fatigue loads calculations of a floating offshore wind turbine". In: *Journal of Physics: Conference Series.* Vol. 2265. 4. Institute of Physics, June 2022. DOI: `10.1088/1742-6596/2265/4/042014`.

[48] [Confidential]. *Metocean Report: Gemini.* Tech. rep. DHI Wasy, 2012.

[49] Decao Yin, Halvor Lie, and Rolf J. Baarholm. "Prototype Reynolds Number VIV Tests on a Full-Scale Rigid Riser". In: *Volume 2: Prof. Carl Martin Larsen and Dr. Owen Oakley Honoring Symposia on CFD and VIV.* American Society of Mechanical Engineers, June 2017. ISBN: 978-0-7918-5764-9. DOI: `10.1115/OMAE2017-61415`.

[50] Philipp R Thies et al. "Accelerated reliability testing of articulated cable bend restrictor for offshore wind applications". In: (2016). DOI: `10.1016/j.ijome.2016.05.006`.

[51] Mary Kathryn Thompson and John M. Thompson. "Introduction to ANSYS and Finite Element Modeling". In: *ANSYS Mechanical APDL for Finite Element Analysis* (Jan. 2017), pp. 1–9. DOI: `10.1016/B978-0-12-812981-4.00001-0`.

[52] Ansys. *Connecting Bolts Represented as Solid Elements Connecting Bolts with the Rest of an Assembly.* Tech. rep. Ansys, 2020. URL: `https://courses.ansys.com/wp-content/uploads/ 2020/09/Connecting-Bolts-Represented-as-Solid-Elements.pdf` (visited on 07/31/2024).

[53] Ansys. *Discovery SpaceClaim.* Tech. rep. 2021. URL: `https://dl.cfdexperts.net/cfd_r esources/Ansys_Documentation/SpaceClaim/SpaceClaim_Documentation.pdf` (visited on 07/31/2024).

[54] DNV-RP-B401. *Cathodic protection design.* DNV, 2021.

[55] ISO 989-1. *Mechanical properties of fasteners made of carbon steel and alloy steel.* International Organization for Standardization, 2013.

[56] Peter Schaumann and Rasmus Eichstadt. "Fatigue Assessment of High Strength Bolts with very Large Diameters in Substructures for Offshore Wind Turbines". In: 2015. ISBN: 9781880653890.

[57] DNV-RP-C208. *Determination of structural capacity by non-linear finite element analysis methods.* DNV, 2019.

[58] Qingmin Yu, Honglei Zhou, and Libin Wang. "Finite element analysis of relationship between tightening torque and initial load of bolted connections". In: *Advances in Mechanical Engineering* 7.5 (May 2015), p. 168781401558847. ISSN: 1687-8140. DOI: `10.1177/1687814015588477`.

[59] R. J.M. Pijpers and H. M. Slot. "Friction coefficients for steel to steel contact surfaces in air and seawater". In: *Journal of Physics: Conference Series.* Vol. 1669. 1. IOP Publishing Ltd, Oct. 2020. DOI: `10.1088/1742-6596/1669/1/012002`.

[60] Ansys. *Ansys Meshing User's guide.* Tech. rep. 2010. URL: `https://www.researchgate.net/ profile/Mohamed-Mourad-Lafifi/post/How_to_remove_warpage_angle_and_violation_of_ heuristic_criterion_warning_in_LS-Dyna/attachment/5d0c0713cfe4a7968dacddf1/AS% 3A771994878496770%401561069330997/download/Meshing_Tutorial_Ans.sys.pdf` (visited on 07/31/2024).

[61]   DNV-RP-F204. *Riser fatigue.* DNV, 2019.

[62]   Ansys. *Modeling the Bolt and Preload.* Tech. rep. 2020. URL: https://courses.ansys.com/index.php/courses/modeling-the-bolt-and-preload/lessons/bolt-pretension-object-lesson-3/.

[63]   Sharda Lochan, Ali Mehmanparast, and John Wintle. "A review of fatigue performance of bolted connections in offshore wind turbines". In: *Procedia Structural Integrity.* Vol. 17. Elsevier B.V., 2019, pp. 276–283. DOI: 10.1016/j.prostr.2019.08.037.

[64]   Terry F. Lehnhoff and Bradley A. Bunyard. "Bolt Thread and Head Fillet Stress Concentration Factors". In: *Recent Advances in Solids and Structures.* American Society of Mechanical Engineers, Nov. 1999, pp. 103–108. ISBN: 978-0-7918-1644-8. DOI: 10.1115/IMECE1999-0620.

[65]   Stipica Novoselac et al. "Fatigue Damage Assessment of Bolted Joint Under Different Preload Forces and Variable Amplitude Eccentric Forces for High Reliability". In: 2017, pp. 239–268. ISBN: 978-3-319-32633-7. DOI: 10.1007/978-3-319-32634-4_13.

[66]   Henk den Besten. "Fatigue damage criteria classification, modelling developments and trends for welded joints in marine structures". In: *Ships and Offshore Structures* 13.8 (Nov. 2018), pp. 787–808. ISSN: 1744-5302. DOI: 10.1080/17445302.2018.1463609.

[67]   Aurélein Geron. *Hands-On Machine Learning with Scikit-Learn, Keras & TensorFlow.* second editon. 2019, pp. 30–32.

[68]   Sotirios V. Archontoulis and Fernando E. Miguez. "Nonlinear Regression Models and Applications in Agricultural Research". In: *Agronomy Journal* 107.2 (Mar. 2015), pp. 786–798. ISSN: 0002-1962. DOI: 10.2134/agronj2012.0506.

[69]   C. Amzallag et al. "Standardization of the rainflow counting method for fatigue analysis". In: *International Journal of Fatigue* 16.4 (1994), pp. 287–293. ISSN: 0142-1123. DOI: https://doi.org/10.1016/0142-1123(94)90343-3. URL: https://www.sciencedirect.com/science/article/pii/0142112394903433.

[70]   J.J. Kauzlarich. "The Palmgren-Miner rule derived". In: *Tribology Series.* 1989, pp. 175–179. DOI: 10.1016/S0167-8922(08)70192-5.

[71]   Leszek Resner and Sandra Paszkiewicz. *Radial water barrier in submarine cables, current solutions and innovative development directions.* 2021. DOI: 10.3390/en14102761.

[72]   J. Bocko, P. Lengvarský, and R. Huňady. "Possibilities of modelling the bolts in program ANSYS". In: *IOP Conference Series: Materials Science and Engineering.* Vol. 776. 1. Institute of Physics Publishing, Apr. 2020. DOI: 10.1088/1757-899X/776/1/012021.

[73]   Fabory. 2024. URL: https://www.fabory.com (visited on 08/13/2024).

A
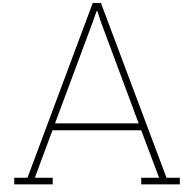
Components Terminology

A.1. Power Cable

Following literature [71] and [14], important components of an array cable, are shown in Figure A.1:
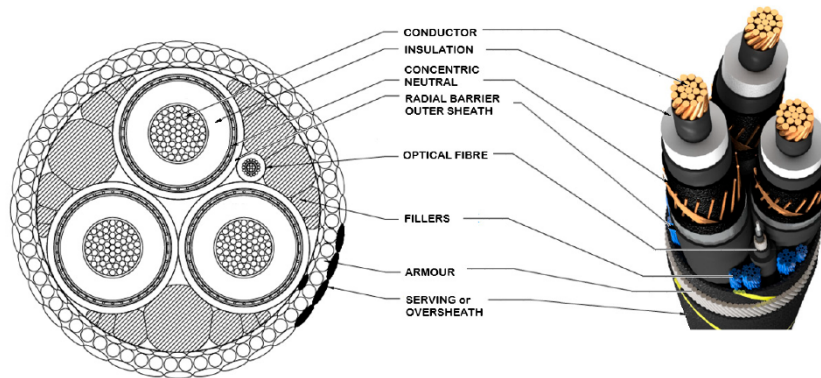
Figure A.1: Example of a common inter-array cable [71]

- **Cable conductor:** Enables the transfer of power.

- Insulation system: including a conductor screen, insulation and an insulation screen (semi-conductive layer). Conductor screen: Material (commonly semiconducting), thickness.

- **Concentric neutral or screen:** To discharge short-circuit currents in the event of cable failure.

- **Radial barrier / outer sheath:** to prevent or significantly diminish ingress of water into the cable insulation and thus to prevent the formation of the water-tree effect, which can lead to cable failure. The outer sheath protects the cable against mechanical damage and performs the function of insulation even to a short circuit.

- **Optical fiber:** for high data transmission capacity for monitoring and control

- **Fillers:** Help lay up the three cable cores and help create a round shape for the cable.

- **Armour:** mainly for the mechanical protection of a subsea cable during its installation and operation.

- **Serving:** To secure the cable during installation, and to secure the armour layer during the process of rewinding and installation.

A.2. Cable Protection System
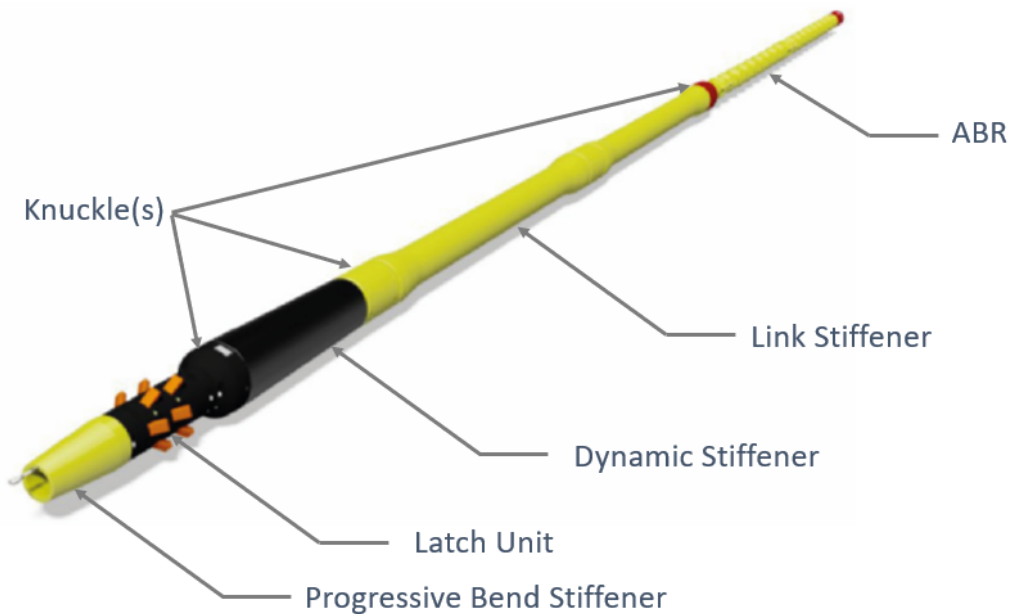
Figure A.2: Example of a Cable Protection System [22]

- **Progressive Bend Stiffener:** this part will be guided through the entry hole and enter the monopile. The purpose of this stiffener is to guide the cable a bit further upwards and provide additional stiffness to prevent it from overbending.

- **Latch Unit:** consists of an assembly of the body and latch fingers. These are designed to latch the CPS to the entry hole. When the latch unit is pulled in the fingers get pushed inside due to the angular shape of the fingers. Once latched, the shape prevents the latch fingers from getting pushed out of the monopile, thereby securing the CPS.

- **Dynamic Stiffener:** is located directly after the latch unit and is therefore exposed to frequent motions since it is relatively far away from the bottom. Just like bend stiffener it provides stiffness to prevent over-bending.

- **Link Stiffeners:** primarily functions similarly to the Dynamic Stiffener by providing additional stiffness. In some CPS designs, Bend Restrictors are used at this location.

- **Bend restrictors:** are designed as a number of interlocking elements and form a semi-rigid curved structure. They are designed to inhibit bending beyond the MBR. These bend restrictors are often half shells that are assembled using bolted joints. The shown example does not show the Bend Restrictors placed directly after the Dynamic Stiffener, however, Figure 2.5 shows an example of such Bend Restrictors.

- **ABR:** is thinner than the bend restrictors and, just like the bend restrictor, is designed to inhibit bending beyond the Minimum Bend Radius (MBR). These ABRs are often a bit more flexible than the previously mentioned Bend Restrictors

- **Knuckles:** are used to connect the different sections with each other. Since the sections vary in design they are not the same. In the model, three knuckles are shown: between the latch unit and the dynamic stiffener, often referred to as latch knuckle, between the dynamic stiffener and the link stiffener and between the link stiffener and the ABR section.

B

Bolt Modelling options in Ansys

Bolt model with real thread The bolt is modelled as a solid body and includes a thread in the geometry. This provides the most accurate results when the mesh is very fine. Modelling however takes longer due to the geometry. The contact between all parts can be defined and friction can be applied.

Bolt model with thread defined in options of contact The bolt is modelled as a solid body and the thread is deleted. However, the bolt thread is defined using the real parameters of the given thread, by using the Ansys option "Contact correction". The pretension effect can still be applied.

Bolt model without thread The bolt is modelled as a solid body and the thread is deleted and the contact behaviour of the thread is not simulated using the "Contact correction" tool. The pretension effect can still be applied. And frictional contact between the bolt and flanges is also still applied.

Bolt model with cylindrical head and nut The bolt is modelled as a solid body, however, the head and nut are now represented without the small faces. The pretension effect can still be applied. And frictional contact between the bolt and flanges is also still applied.

Bolt model with cylindrical head and nut, and cylindrical joint contact The bolt is modelled as a solid body, and again the head and nut are represented without faces. The difference with this model is that the thread parameters will be defined using the "Commands" tool in Ansys.

Bolt model as line body with bonded contact and imprint faces 3D solid body is replaced by a line body, with the same diameter as the bolt. The bonded contact functions to have a connection between the flanges and the line body. One the upper end of the line is connected with the imprint face of the flange and the lower end is connected within the lower imprint face of the flange.

Bolt model as a line body 3D solid body is replaced by a line body, with the same diameter as the bolt. The bonded contact functions to have a connection between the flanges and the line body. The model is simplified by neglecting the imprint faces.

Bolt model without solid and line body The bolt is not modelled as a solid in the geometry step, but simulated as a beam connector from body to body, therefor it has figure.

Bolt figures are obtained from [72]
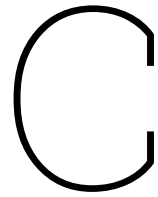
Bolt Assembly Dimensions

b (min.): 125mmL≤200mm	44
b (min.): L200mm	57
b (min.): L≤125mm	38
d-D	M16
k	10
L (mm)	110
P	2
s	24
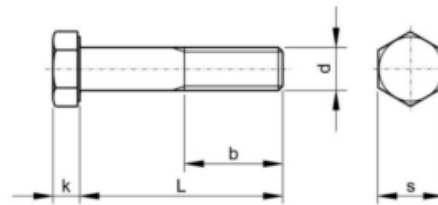
Figure C.1: DIN 931 Bolt [73]

d-D	M16
m	13
P	2
s	24
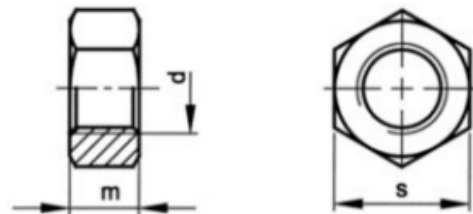
Figure C.2: DIN 934 Nut [73]

d1	17
d2	30
h	3
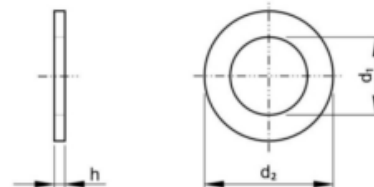
Figure C.3: DIN 125-1A Washer [73]

D

Total Damage per Direction

Hs / Tp	4	6	8	10	12	14	SUM
9.00	0	0	0	0	1.44e-11	1.79e-10	1.94e-10
8.00	0	0	0	1.35e-12	3.59e-10	6.74e-11	4.28e-10
7.00	0	0	0	0	4.09e-11	4.10e-11	8.20e-11
6.00	0	0	0	0	0	1.10e-11	1.10e-11
5.00	0	0	0	0	0	0	0
4.00	0	0	0	0	0	0	0
3.00	0	0	0	0	0	0	0
2.00	0	0	0	0	0	0	0
1.00	0	0	0	0	0	0	0
SUM	0	0	0	1.35e-12	4.14e-10	2.98e-10	7.15e-10

Table D.1: Total Damage 90 degrees

Hs / Tp	4	6	8	10	12	14	SUM
9.00	0	0	0	0	3.88e-13	9.59e-12	9.98e-12
8.00	0	0	0	0	2.97e-11	7.77e-12	3.74e-11
7.00	0	0	0	0	1.12e-11	1.40e-12	1.26e-11
6.00	0	0	0	0	0	3.81e-12	3.81e-12
5.00	0	0	0	0	0	0	0
4.00	0	0	0	0	0	0	0
3.00	0	0	0	0	0	0	0
2.00	0	0	0	0	0	0	0
1.00	0	0	0	0	0	0	0
SUM	0	0	0	0	4.13e-11	2.26e-11	6.38e-11

Table D.2: Total Damage 120 degrees

Hs / Tp	4	6	8	10	12	14	SUM
9.00	0	0	0	0	6.38e-11	2.95e-10	3.59e-10
8.00	0	0	0	6.04e-12	3.84e-10	2.06e-10	5.95e-10
7.00	0	0	0	0	1.01e-10	1.24e-10	2.26e-10
6.00	0	0	0	0	1.42e-11	3.20e-11	4.62e-11
5.00	0	0	0	0	0	2.16e-12	2.16e-12
4.00	0	0	0	0	0	0	0
3.00	0	0	0	0	0	0	0
2.00	0	0	0	0	0	0	0
1.00	0	0	0	0	0	0	0
SUM	0	0	0	6.04e-12	5.63e-10	6.59e-10	1.23e-09

Table D.3: Total Damage 150 degrees

Hs / Tp	4	6	8	10	12	14	SUM
9.00	0	0	0	0	4.49e-10	7.20e-09	7.65e-09
8.00	0	0	0	2.46e-11	3.84e-09	8.85e-10	4.75e-09
7.00	0	0	0	8.56e-11	2.58e-09	2.26e-10	2.89e-09
6.00	0	0	0	0	4.09e-10	2.23e-10	6.32e-10
5.00	0	0	0	0	7.47e-11	1.67e-11	9.15e-11
4.00	0	0	0	0	0	0	0
3.00	0	0	0	0	0	0	0
2.00	0	0	0	0	0	0	0
1.00	0	0	0	0	0	0	0
SUM	0	0	0	1.10e-10	7.35e-09	8.55e-09	1.60e-08

Table D.4: Total Damage 180 degrees

Hs / Tp	4	6	8	10	12	14	SUM
9.00	0	0	0	0	2.53e-10	1.48e-09	1.73e-09
8.00	0	0	0	1.76e-11	5.98e-09	7.40e-10	6.74e-09
7.00	0	0	0	0	4.64e-10	4.74e-10	9.38e-10
6.00	0	0	0	0	2.38e-10	1.31e-10	3.69e-10
5.00	0	0	0	0	0	3.43e-12	3.43e-12
4.00	0	0	0	0	0	0	0
3.00	0	0	0	0	0	0	0
2.00	0	0	0	0	0	0	0
1.00	0	0	0	0	0	0	0
SUM	0	0	0	1.76e-11	6.93e-09	2.83e-09	9.78e-09

Table D.5: Total Damage 210 degrees

Hs / Tp	4	6	8	10	12	14	SUM
9.00	0	0	0	0	1.08e-12	2.47e-11	2.58e-11
8.00	0	0	0	0	0	0	0
7.00	0	0	0	0	0	0	0
6.00	0	0	0	0	0	0	0
5.00	0	0	0	0	0	0	0
4.00	0	0	0	0	0	0	0
3.00	0	0	0	0	0	0	0
2.00	0	0	0	0	0	0	0
1.00	0	0	0	0	0	0	0
SUM	0	0	0	0	1.08e-12	2.47e-11	2.58e-11

Table D.6: Total Damage 240 degrees

Hs / Tp	4	6	8	10	12	14	SUM
9.00	0	0	0	0	2.47e-12	6.31e-11	6.55e-11
8.00	0	0	0	0	3.22e-11	6.02e-12	3.82e-11
7.00	0	0	0	0	0	6.43e-12	6.43e-12
6.00	0	0	0	0	0	0	0
5.00	0	0	0	0	0	0	0
4.00	0	0	0	0	0	0	0
3.00	0	0	0	0	0	0	0
2.00	0	0	0	0	0	0	0
1.00	0	0	0	0	0	0	0
SUM	0	0	0	0	3.47e-11	7.55e-11	1.10e-10

Table D.7: Total Damage 270 degrees

E
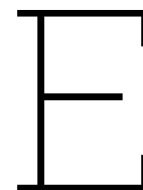
Python Codes

E.1. Regression Model

```python
1  import pandas as pd
2  import numpy as np
3  from sklearn.model_selection import train_test_split
4  from sklearn.preprocessing import PolynomialFeatures
5  from sklearn.linear_model import LinearRegression
6
7  # Load your dataset
8  df = pd.read_csv("1000caseskN.csv")
9  X = df[['ztension', 'general shear force', 'general bend moment']]
10 y = df['WL_NR']
11
12 X.columns = ['x0', 'x1', 'x2']
13
14 # Split the data into training and testing sets (80% train, 20% test)
15 X_train, X_test, y_train, y_test = train_test_split(X, y, test_size=0.2, random_state=42)
16
17 # Create polynomial features
18 poly = PolynomialFeatures(degree=2, include_bias=False)
19 X_train_poly = poly.fit_transform(X_train)
20 X_test_poly = poly.transform(X_test)
21
22 # Fit the polynomial regression model
23 poly_regr = LinearRegression()
24 poly_regr.fit(X_train_poly, y_train)
25
26 # Retrieve the coefficients and intercept
27 coefficients = poly_regr.coef_
28 intercept = poly_regr.intercept_
29
30 # Get feature names
31 feature_names = poly.get_feature_names_out(['x0', 'x1', 'x2'])
32
33 # Replace ^ with ** in feature names
34 feature_names = [name.replace(' ', '*').replace('^', '**') for name in feature_names]
35
36 # Construct the polynomial formula as a string
37 formula = f"{intercept:.4f}"
38 for coef, name in zip(coefficients, feature_names):
39     formula += f" + ({coef:.4f})*{name}"
40
41 print("Polynomial Formula:")
42 print(formula)
43
44 # Evaluate the model
45 mse = mean_squared_error(y_test, y_pred)
46 r2 = r2_score(y_test, y_pred)
47
```

```python
48  # Calculate the adjusted R-squared
49  n = X_test_poly.shape[0]
50  p = X_test_poly.shape[1]
51  adjusted_r2 = 1 - ((1 - r2) * (n - 1) / (n - p - 1))
52
53  print("Mean␣Squared␣Error␣(MSE):␣{:.2f}".format(mse))
54  print("R-squared␣(R²):␣{:.2f}".format(r2))
55  print("Adjusted␣R-squared:␣{:.2f}".format(adjusted_r2))
```

E.2. OrcaFlex External Function

```python
1
2  import json
3  import math
4  import OrcFxAPI
5  import numpy as np
6
7
8  # Only one external result calculated by this external function
9  STRESS_RESULT_ID = 0
10
11 class NodeHalfSegmentData(object):
12     # A helper class for storing half segment working data
13     def __init__(self):
14         self.curv_x_y = (0.0, 0.0)
15         self.arclength = -1.0
16         self.segmentIn = False
17
18 class StressFactor(object):
19     def __init__(self):
20         # Create a period object once in this instance for reuse later.
21         self.INSTANTANEOUS_PERIOD = OrcFxAPI.Period(OrcFxAPI.pnInstantaneousValue)
22
23     def Initialise(self, info):
24         # Two instances of this external result are created for each line node, one for each
                half segment
25         # - In and Out. The DataName tells us which half segment we are in which we store in
                a WorkingData object.
26         self.WorkingData = NodeHalfSegmentData()
27         self.WorkingData.segmentIn = True if info.DataName.endswith("In") else False
28
29     def RegisterResults(self, info):
30         # Pass OrcaFlex some details of the result we are calculating. The result 'ID' is
                used by OrcaFlex to
31         # specifiy the result required when calling 'DeriveResult' below. The units code
                string '$S' will be
32         # substituted by OrcaFlex with the stress units used by the model.
33         info.ExternalResults = [{"ID": STRESS_RESULT_ID, "Name": "Bolt␣Stress", "Units": "$S"
                }]
34
35     def TrackCalculation(self, info):
36         # Called before LogResult, this method gives the External Result instance a chance to
                 view the value
37         # for the data item, the instantaneous calculation data and update our working data.
                We record the
38         # mid segment arclength for this node here as this information is not available in
                the Initialise call.
39         # We also record the x and y curvature components for the half segment at this time
                step and record
40         # this in our working data. This method is called twice for each Node at each log
                interval.
41         wd = self.WorkingData
42         nodeData = info.InstantaneousCalculationData
43         if wd.arclength < 0.0:  # If the arclength in the working data has not been
                initialised - do so.
44             wd.arclength = nodeData.MidSegArcLengthIn if wd.segmentIn else nodeData.
                    MidSegArcLengthOut
45         wd.curv_x_y = nodeData.CurvatureIn if wd.segmentIn else nodeData.CurvatureOut
46         #
47
```

```python
48      def LogResult(self, info):
49          wd = self.WorkingData
50          current_arclength = wd.arclength
51          # Determine the arclength of the adjacent node (one segment away)
52          #adjacent_arclength = (current_arclength - 10.899) # 0.1 is to compensate for the
                middle of the segment Taken from point B (19.763) - 16.099= 3.664 (point of
                interest)
53          adjacent_arclength = (current_arclength - 10.889)
54          # Create ArcLength objects for the current and adjacent nodes
55          current_oe = OrcFxAPI.oeArcLength(current_arclength)
56          adjacent_oe = OrcFxAPI.oeArcLength(adjacent_arclength)
57          # Retrieve data for the current node
58          tension = info.ModelObject.TimeHistory("Effective␣tension", self.INSTANTANEOUS_PERIOD
                , current_oe)[0]
59          x_shear = info.ModelObject.TimeHistory("x␣shear␣force", self.INSTANTANEOUS_PERIOD,
                current_oe)[0]
60          y_shear = info.ModelObject.TimeHistory("y␣shear␣force", self.INSTANTANEOUS_PERIOD,
                current_oe)[0]
61          x_moment = info.ModelObject.TimeHistory("x␣bend␣moment", self.INSTANTANEOUS_PERIOD,
                current_oe)[0]
62          y_moment = info.ModelObject.TimeHistory("y␣bend␣moment", self.INSTANTANEOUS_PERIOD,
                current_oe)[0]
63          # Retrieve data for the adjacent node
64          adjacent_tension = info.ModelObject.TimeHistory("Effective␣tension", self.
                INSTANTANEOUS_PERIOD, adjacent_oe)[0]
65          adjacent_x_shear = info.ModelObject.TimeHistory("x␣shear␣force", self.
                INSTANTANEOUS_PERIOD, adjacent_oe)[0]
66          adjacent_y_shear = info.ModelObject.TimeHistory("y␣shear␣force", self.
                INSTANTANEOUS_PERIOD, adjacent_oe)[0]
67          adjacent_x_moment = info.ModelObject.TimeHistory("x␣bend␣moment", self.
                INSTANTANEOUS_PERIOD, adjacent_oe)[0]
68          adjacent_y_moment = info.ModelObject.TimeHistory("y␣bend␣moment", self.
                INSTANTANEOUS_PERIOD, adjacent_oe)[0]
69          # Store the data in the LogData attribute
70          info.LogData = json.dumps([tension, x_shear, y_shear, x_moment, y_moment,
                adjacent_tension, adjacent_x_shear, adjacent_y_shear, adjacent_x_moment,
                adjacent_y_moment])
71
72
73
74      def DeriveResult(self, info):
75          if info.ResultID == STRESS_RESULT_ID:
76              # Retreive our logged data, and use the json module to convert the string back to
                    Python types.
77              logData = json.loads(info.LogData)
78              tension = logData[0]
79              x_shear = logData [1]
80              y_shear = logData [2]
81              x_moment = logData [3]
82              y_moment = logData [4]
83              adjacent_tension = logData [5]
84              adjacent_x_shear = logData [6]
85              adjacent_y_shear = logData [7]
86              adjacent_x_moment = logData[8]
87              adjacent_y_moment = logData[9]
88              x0 = adjacent_tension
89              x1 = np.sqrt(adjacent_x_shear**2 + adjacent_y_shear**2)
90              x2 = np.sqrt(adjacent_x_moment**2 + adjacent_y_moment**2)
91              # Load in the user specified parameters for the external result in the
                    objectextra's
92              # ExternalResultText property. We are also using the JSON format for this text.
93              # Calculate and return the stress component result to OrcaFlex
94              info.Value = (((101.4656 + (6.2988)*x0 + (0.3074)*x1 + (-5.4864)*x2 + (0.5868)*x0
                    **2 + (-0.3734)*x0*x1 + (-0.4080)*x0*x2 + (0.0862)*x1**2 + (-0.1051)*x1*x2 +
                    (0.2695)*x2**2)/0.157)*1000)
95  print(STRESS_RESULT_ID)
```